Catalysis in a Cage: Condition-Dependent Speciation and Dynamics of Exchanged Cu Cations in SSZ-13 Zeolites

Christopher Paolucci,[†] Atish A. Parekh,[‡] Ishant Khurana,[‡] John R. Di Iorio,[‡] Hui Li,[†] Jonatan D. Albarracin Caballero,[‡] Arthur J. Shih,[‡] Trunojoyo Anggara,[†] W. Nicholas Delgass,[‡] Jeffrey T. Miller,[‡] Fabio H. Ribeiro,[‡] Rajamani Gounder,[‡] and William F. Schneider*,[†]

[†]Department of Chemical and Biomolecular Engineering, University of Notre Dame, 182 Fitzpatrick Hall, Notre Dame, Indiana 46556, United States

[‡]School of Chemical Engineering, Purdue University, 480 Stadium Mall Drive, West Lafayette, Indiana 47907, United States

S *Supporting Information*

ABSTRACT: The relationships among the macroscopic compositional parameters of a Cu-exchanged SSZ-13 zeolite catalyst, the types and numbers of Cu active sites, and activity for the selective catalytic reduction (SCR) of NO_x with NH_3 are established through experimental interrogation and computational analysis of materials across the catalyst composition space. Density functional theory, stochastic models, and experimental characterizations demonstrate that within the synthesis protocols applied here and across Si:Al ratios, the volumetric density of six-membered-rings (6MR)

containing two Al (2Al sites) is consistent with a random Al siting in the SSZ-13 lattice subject to Löwenstein's rule. Further, exchanged Cu^{II} ions first populate these 2Al sites before populating remaining unpaired, or 1Al, sites as $Cu^{II}OH$. These sites are distinguished and enumerated ex situ through vibrational and X-ray absorption spectroscopies (XAS) and chemical titrations. In situ and operando XAS follow Cu oxidation state and coordination environment as a function of environmental conditions including low-temperature (473 K) SCR catalysis and are rationalized through first-principles thermodynamics and ab initio molecular dynamics. Experiment and theory together reveal that the Cu sites respond sensitively to exposure conditions, and in particular that Cu species are solvated and mobilized by NH_3 under SCR conditions. While Cu sites are spectroscopically and chemically distinct away from these conditions, they exhibit similar turnover rates, apparent activation energies and apparent reaction orders at the SCR conditions, even on zeolite frameworks other than SSZ13.
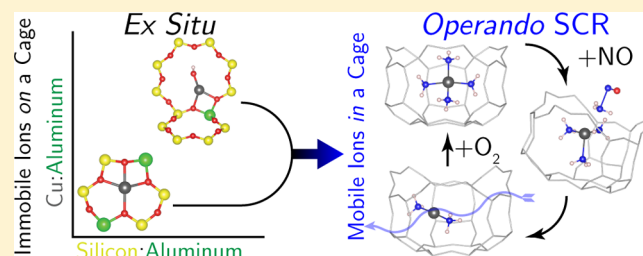
1. INTRODUCTION

In 1925,[1] Hugh Stott Taylor theorized that specific groups of atoms were responsible for the rate-enhancing capacity of heterogeneous catalyst surfaces, from which he coined the phrase "active site". This concept has become ubiquitous in modern catalysis science and has proven indispensable to the emergence of rational catalyst design. Most catalytic solids, however, are structurally heterogeneous at the molecular scale. They contain a distribution of active sites of different catalytic reactivity,[2−4] reflecting nonuniformities in active site coordination and local environment,[5,6] response to external stimuli,[7,8] and interactions with reacting molecules.[9−12] The integration of density functional theory (DFT) computational models and experimental operando spectroscopies that interrogate active sites during catalysis can provide powerful insights into the coupling between active site composition, reaction environment, and reaction mechanism.[13,14] In this work, we demonstrate how this approach enables the identification, quantification, and characterization of distinctly different active sites in a macro- and microscopically heterogeneous zeolite catalyst. We show through operando characterization that the composition and structure of active sites change dynamically during reaction, differ from their ex situ states, and that such reaction-environment-induced modifications are integral to observed catalytic performance.

We demonstrate this capability in the context of Cu-exchanged zeolite catalysts. Zeolites are crystalline, nanoporous aluminosilicates constructed of corner-sharing SiO_4 and AlO_4 tetrahedra, or T-sites. Framework substitution of Si^{4+} by Al^{3+} introduces an anionic charge into the oxide lattice that must be charge-compensated by extralattice cations. The Al sites are in general not ordered, so that at a given Si:Al ratio a zeolite presents a distribution of local Al environments.[15−19] The common oxidation states of Cu are 1+ and 2+, and thus a single Cu ion can in principle charge-compensate one or two Al T-sites.[20−27] The exact form of this exchange and charge compensation can depend on Cu oxidation state, overall framework structure, and local Al siting. In addition, Cu is observed to form multinuclear oxo-complexes and oxide

clusters that further enrich its exchange chemistry and catalysis.[28−33]

Cu-exchanged zeolites have been explored for a variety of hydrocarbon partial oxidations[31,32,34−44] and NO$_x$ reduction and decomposition chemistries.[45−47] Cu-zeolites have long been known to be active for the selective catalytic reduction (SCR) of NO$_x$ with NH$_3$.[13,48−56] SCR catalysts promote the reduction of NO$_x$ by NH$_3$:

$$4NH_3 + 4NO + O_2 \rightarrow 6H_2O + 4N_2 \qquad (1)$$
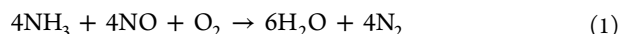
over the competing and undesired oxidation of NH$_3$:

$$4NH_3 + 3O_2 \rightarrow 6H_2O + 2N_2 \qquad (2)$$
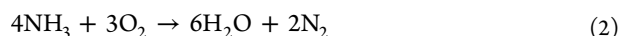
Small pore Cu-exchanged SSZ-13, in particular, is able to satisfy all of the practical requirements of an SCR catalyst and is now in commercial use.[57−60] However, the relationships between zeolite composition, reaction conditions, active site(s), and mechanism remain to be elucidated.

SSZ-13 has the chabazite topology. The single symmetry-distinct T-site organizes into four-, six-, and eight-membered rings (Figure 1, left) that form a cage ∼8 Å in diameter.[61] SSZ-
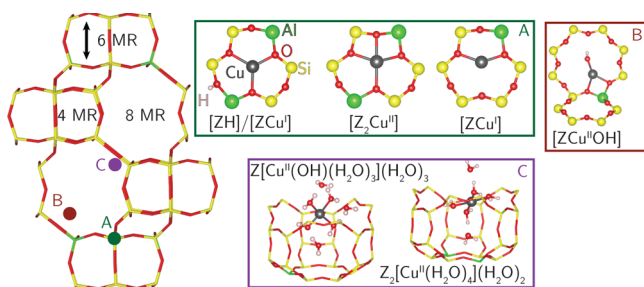

Figure 1. (left) Side view of the chabazite cage. (right) HSE06-optimized structures of (A,B) dehydrated oxidized and reduced Cu sites and (C) hydrated oxidized sites. Label indicates location of Cu ion within the chabazite cage.

13 can be prepared in elemental compositions from highly enriched (Si:Al = 2) to infinitely dilute (Si:Al = ∞) in Al sites. The H-form (i.e., Al charge-compensated by H$^+$) can be exchanged to various Cu:Al ratios, and the locations and forms of these exchanged Cu ions have received considerable attention.[28,62,63,65−79] X-ray absorption (XAS), UV−visible (UV−vis), and infrared (IR) spectra of zeolites[28,42,66,70,71,80,81] all suggest exchanged Cu ions are present as hydrated and oxidized Cu^{II}(H$_2$O)$_6$[82] at ambient conditions regardless of zeolite composition and topology.

The homogeneity of Cu sites under ambient conditions gives way to a rich variety of Cu species after high temperature and oxidative removal of H$_2$O. X-ray diffraction (XRD) reveals monomeric Cu ions in SSZ-13 that occupy either 6MR (A) sites[63,69] or both (A) and (B) sites[62,75] (Figure 1). We have reported that high Al content Cu-SSZ-13 zeolites (Si:Al = 5) contain exclusively Cu^{II} in the (A) site under dry oxidizing conditions up to a Cu:Al = 0.20,[66,83] as demonstrated through the 4-fold coordination of Cu with zeolitic oxygen in extended X-ray absorption fine structure spectra (EXAFS) and titrations of residual Brønsted acid sites that reveal a 2:1 H$^+$:Cu^{2+} exchange stoichiometry. In contrast, Borfecchia et al. report 3-fold Cu coordination under similar conditions[64] on a Si:Al = 13, Cu:Al = 0.44 sample. Giordanino et al. report IR features attributable to Cu hydroxyl ([Cu^{II}OH]$^+$)[64,71] on Si:Al = 13, Cu:Al = 0.44, whereas Gao et al. only observe this band on a

subset of Si:Al = 6 samples.[76] DFT calculations generally indicate that isolated, unligated Cu^I and Cu^{II} ions prefer the A site (Figure 1, left) regardless of the location of Al.[64,66,68,83−88]

H$_2$ temperature-programmed reduction (TPR)[76,89] experiments are consistent with the existence of at least two types of exchanged Cu^{II} with differing susceptibility to reduction. Borfecchia et al. similarly observe only a fraction of Cu^{II} ions to reduce in He at 673 K. Chemical probes including NO, NO$_2$, and CO[73,89−94] will thus see a different mixture of Cu sites depending on sample history. For instance, NO adsorbs strongly on vacuum-reduced Cu^{II} → Cu^I sites[89,90] but more weakly and dynamically on Cu^{II} sites.[65,83] The relevance of these ex situ probes to catalytic conditions has yet to be established.

Standard SCR is a redox reaction, as evidenced by the observation of both Cu^I and Cu^{II} in operando experiments,[73,84,95] and thus the ex situ reducibility of catalysts might be expected to correlate with observed activity. However, catalysts with different ex situ properties exhibit similar SCR characteristics. Reactant cutoff experiments demonstrate that both NO and NH$_3$ are necessary for the Cu^{II} → Cu^I reduction half-cycle across samples of various compositions.[73,83] Apparent activation energies are the same (∼70 kJ mol^{-1}), and 473 K SCR turnover rates are linear in Cu content (Cu:Al = 0.08−0.20) on Si:Al = 5 samples.[66,83,96] Samples with compositions nearer to those studied by Borfecchia et al. present the same Cu^I/Cu^{II} fractions in operando XAS[73] and apparent activation energies[76] similar to those of the Si:Al = 5 samples but different susceptibilities to Cu reduction in H$_2$ TPR.[76]

Thus, while there is general agreement that various isolated, exchanged Cu ions are present and contribute to the SCR catalysis, the precise nature, number, and reactivity of different cationic species, their dependence on zeolite composition (Si:Al and Cu:Al ratios) and framework topology, sample treatment history and environment, and their spectroscopic signatures under ex situ versus in situ conditions remain unknown. Here, we report a coordinated computational (stochastic simulation, ab initio dynamics, and free energy) and experimental (synthetic, spectroscopic, and titrimetric) analysis of Cu speciation under ex situ conditions and in situ and operando SCR conditions as a function of catalyst composition over a wide range of zeolite chemical composition space. We demonstrate that the types, numbers, and chemical characteristics of Cu sites depend on bulk composition of the zeolite, can be predicted through first-principles-based models, can be distinguished in the laboratory, and depend strongly on the environmental conditions. Environmental conditions have a profound impact on Cu ion siting, coordination, and mobility, resulting in SCR turnover rates (473 K) that are independent of the initial Cu cation site and the zeolite framework type. The results rationalize a large body of literature, resolve contradictory findings regarding the active sites for NO$_x$ SCR, and consolidate the understanding of Cu cation speciation in zeolites.

2. RESULTS

2.1. Cu Cation Speciation in Cu-SSZ-13. *2.1.1. First-Principles Speciation of Cationic Cu Complexes.* We first created molecular models for isolated Cu exchange sites in SSZ-13 and established their relative free energies under wet and oxidizing conditions relevant to Cu exchange and catalyst treatment; computational details can be found in section 5.1. We used a 12 T-site supercell[66,83,84] with a single Al
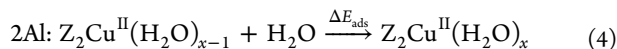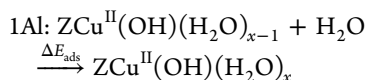
substitution to represent an isolated Al atom in the CHA framework. Charge-compensating Cu^I ions prefer to sit in the plane of the 6MR,[66,83,84,86] and we label this structure as $[ZCu^I]$ in Figure 1A to denote charge-compensation of a single Al (Z) by Cu. This notation also emphasizes the formal 1+ oxidation state of Cu, and this structure is used as the Cu^I reference in relating computed Bader charges to effective Cu oxidation states. An oxidized form of the Cu site compensating a single framework Al atom has been proposed[64,72,73] to be formed by addition of an extra-lattice OH ligand, which redirects the Cu into the 8MR according to the optimized $[ZCu^{II}OH]$ structure shown in Figure 1B.

Similarly, two proximal framework Al atoms (2Al sites) can be charge compensated by a single Cu^{II} ion. The exchange energies of Cu^{II} at different potential 2Al sites were previously computed using a $2 \times 1 \times 1$ 24 T-site supercell containing 4 Al atoms distributed to place 2Al sites in each of the 4, 6, and 8MR:[66]

$$Z_4H_4 + Cu^{II}_{(aq)} \rightarrow Z_4H_2Cu^{II} + 2H^+_{(aq)} \quad (3)$$
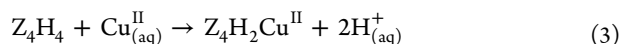
Cu^{II} exchange at 2Al sites in the 6MR ring is 108 and 145 kJ mol^{-1} more exothermic than exchange at 2Al sites in the 4MR and 8MR, respectively. We adopt a model with 2Al at third-nearest-neighbor (3NN) positions in a 6MR for Cu near 2Al. Cu exchange at the 2NN Al 6MR is coordinatively similar and the exchange energy more endothermic by 22 kJ mol^{-1}. The 3NN Al 6MR structure is labeled $[Z_2Cu^{II}]$ in Figure 1A and is taken as the Bader charge standard for the Cu^{II} oxidation state. We previously found that this $[Z_2Cu^{II}]$ site can be reduced by addition of H to an Al site proximal to Cu,[83] which is the $[ZH]/[ZCu^I]$ species shown in Figure 1A. The forward slash emphasizes that these two sites are proximal. Reduction to Cu^I decreases Cu coordination to the lattice but preserves Cu location within the 6MR.

Motivated by XAS[20,66,70] and molecular dynamics[97] evidence that exchanged Cu^{II} ions are hydrated under ambient conditions, we first explored H_2O coordination to the $[Z_2Cu^{II}]$ and $[ZCu^{II}OH]$ ions by computing the structures and successive adsorption energies of H_2O ligands ($x = 1-6$):

$$1Al: ZCu^{II}(OH)(H_2O)_{x-1} + H_2O \xrightarrow{\Delta E_{ads}} ZCu^{II}(OH)(H_2O)_x$$

$$2Al: Z_2Cu^{II}(H_2O)_{x-1} + H_2O \xrightarrow{\Delta E_{ads}} Z_2Cu^{II}(H_2O)_x \quad (4)$$

In each simulation, we started from the equilibrated ($x - 1$) H_2O structure, added another H_2O molecule, annealed for 150 ps at 473 K using NVT ab initio molecular dynamics (AIMD) at the GGA level, then subsequently optimized the geometry and evaluated the energy with the HSE06 functional including Tkatchenko Scheffler van der Waals (TSvdw) corrections (section 5.1), and zero-point vibrational energies (ZPE) (Supporting Information 2.1.1-1). Energy and Cu coordination number (CN) results are summarized in Table 1, where CN is defined as the number of heavy atoms within 2.3 Å of Cu. H_2O adsorption energies are on the order of −70 to −90 kJ mol^{-1} and are generally more exothermic on $[Z_2Cu^{II}]$ than on $[ZCu^{II}OH]$ sites. The computed Cu oxidation state is insensitive to added H_2O. On $[Z_2Cu^{II}]$, successive H_2O ligands generally displace framework oxygen (O_f) from the first coordination sphere, until at $x = 4$ the Cu^{II} ion is fully coordinated by H_2O; additional H_2O molecules form a second coordination sphere through hydrogen bonds to first shell H_2O.

**Table 1. H_2O Adsorption Energies (ΔE_{ads}) on Cu Sites Computed Using HSE06-TSvdw[a]**

	+xH$_2$O	1	2	3	4	5	6
Z$_2$Cu	ΔE_{ads} (kJ mol^{-1})	−84	−94	−108	−84	−90	−73
	cage location	A	A	B	C	C	C
	O$_f$/total CN	3/4	3/4	2/4	0/4	0/4	0/4
ZCuOH	ΔE_{ads} (kJ mol^{-1})	−75	−67	−76	−63	−95	−56
	cage location	B	C	C	C	C	C
	O$_f$/total CN	2/4	0/3	0/3	0/4	0/4	0/4

[a]Cage location referenced to Figure 1. CN and O$_f$ indicate total Cu coordination number and number of close framework O contacts, respectively.

With hydration, the Cu ion moves from within the 6MR (site A, Figure 1) to the 8MR (site B) to the cage center (site C). The final optimized $x = 6$ structure is shown in Figure 1C. The $[ZCu^{II}OH]$ site behaves similarly with added H_2O; the fully hydrated complex is shown in Figure 1C.

Exchanged Cu may lose waters of hydration and acquire other ligands during synthesis and after oxidation or reduction treatments. We computed the structures and energies of various combinations of O, OH, H_2O, and O_2 ligands on both the 1Al and the 2Al models in the nominally oxidized and reduced states. The list of candidate structures was guided by chemical plausibility and includes proposed intermediate species reported elsewhere (e.g., $Cu^{II}O$, $Cu^{II}(OH)_2$).[84,98] Optimized structures, energies, and ZPEs of all 26 species are tabulated in Supporting Information 2.1.1-1.

We applied a first-principles thermodynamic analysis to rank the stability of this library of Cu-bound H_xO_y species as a function of temperature and hydrogen and oxygen potentials. We take O_2 and H_2O as the oxygen and hydrogen references, respectively:

$$Z_*Cu + \frac{x}{2}\left(H_2O - \frac{1}{2}O_2\right) + \frac{y}{2}O_2 \xrightarrow{\Delta G_{form}} Z_*CuH_xO_y \quad (5)$$
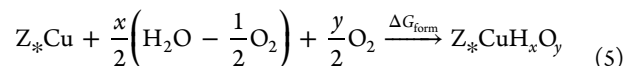
used the HSE06-TSvdw energies, and applied previously developed correlations[83] to estimate adsorbate entropies. The formation free energies (ΔG_{form}) are computed according to section 5.2 and the μ_{H_2O} and μ_{O_2} related to T and P through the ideal gas relation. Results for an ambient condition (condition 1, 298 K, 2% H_2O, and 20% O_2) representative of an air-exposed catalyst and an elevated temperature condition (condition 2, 673 K, 2% H_2O, and 20% O_2) representative of an oxidation pretreatment are summarized in Figure 2. For clarity, species with $\Delta G_{form} > +200$ kJ mol^{-1} are not shown in condition 2. The relative energy alignment between Cu near 1Al and 2Al is described in section 2.1.2.

At the high temperatures (673 K) and high oxygen potentials (20% O_2) of condition 2, the lowest free energy structure near the 2Al site is the isolated $[Z_2Cu^{II}]$ ion. At these conditions, adsorption of a single H_2O ligand is endergonic by 15 kJ mol^{-1}, and the reduced form of the Cu site ($[ZCu^I]/[ZH]$) is endergonic by another 15 kJ mol^{-1}. Other adsorbates on Cu sites near 2Al lead to complexes much higher in free energy, including adsorbed molecular O_2. Similarly, on Cu sites near 1Al, the lowest free energy structure is oxidized $[ZCu^{II}OH]$ with normalized Bader charge (Supporting Information 2.1.1-1) of +1.8, slightly less than $[Z_2Cu^{II}]$. The reduced form of the site, $[ZCu^I]$, and its hydrated form, $[ZCu^I(H_2O)]$, are very
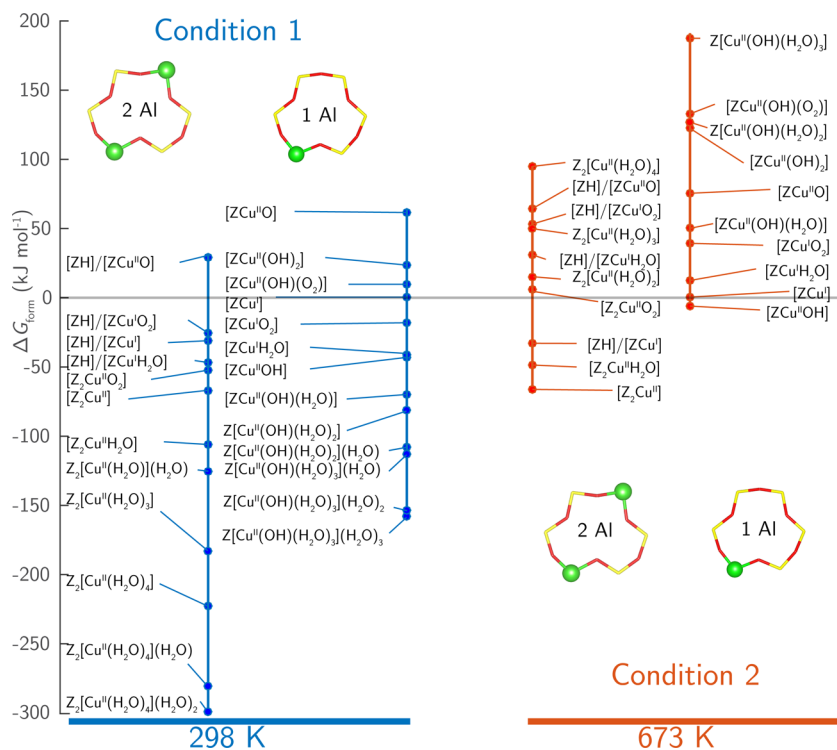
Figure 2. Formation free energies (ΔG_{form}) CuH$_x$O$_y$ species at (left) 298 K, 2% H$_2$O, 20% O$_2$, and at (right) 673 K, 2% H$_2$O, 20% O$_2$ on the 2Al (Z$_2$Cu) and 1Al (ZCu) sites. Common energy reference set through eq 6.
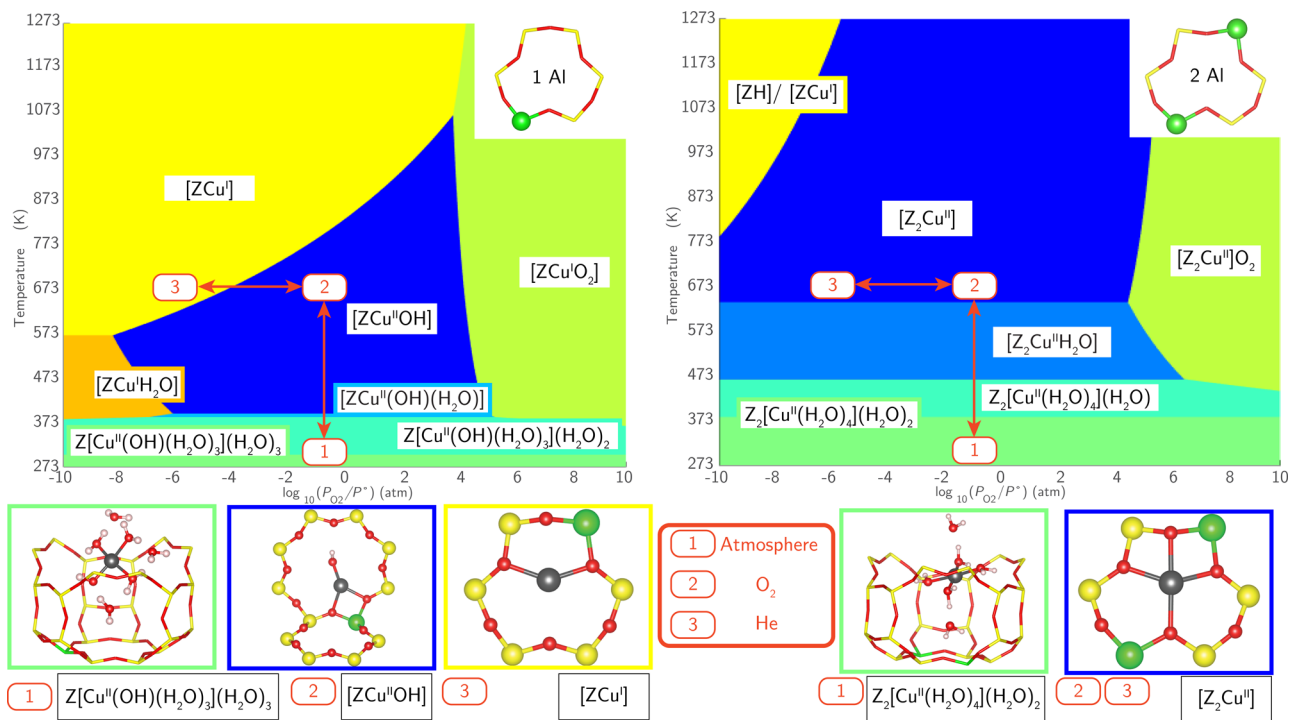

Figure 3. Ex situ Cu speciation phase diagrams based on HSE06-Tsvdw calculations on 1Al (left) and 2Al (right) Cu exchange sites. Regions indicate site composition that minimizes free energy at 2% H$_2$O and given T and P_{O_2}. Labeled on the phase diagram and illustrated below are minimum free energy species at (1) ambient (298 K, 20% O$_2$), (2) oxidizing (673 K, 20% O$_2$), and (3) inert (673 K, 10^{-6} atm O$_2$ in He).

close in free energy to the oxidized [ZCu^{II}OH] state. Molecular O$_2$ adsorption on the [ZCu^I] site is endergonic by 50 kJ mol^{-1} relative to [ZCu^{II}OH], and even higher in free energy are other oxidized forms, including [ZCu^{II}O][98] and [ZCu^{II}(OH)$_2$].[84] The primary effect of decreasing temperatures to ambient

(condition 1) is a significant decrease in the free energies of all hydrated Cu states, which causes the most stable species to become the fully hydrated Z$_2$[Cu^{II}(H$_2$O)$_4$](H$_2$O)$_2$ and Z-[Cu^{II}(OH)(H$_2$O)$_3$](H$_2$O)$_3$ complexes at 2Al and 1Al sites, respectively.
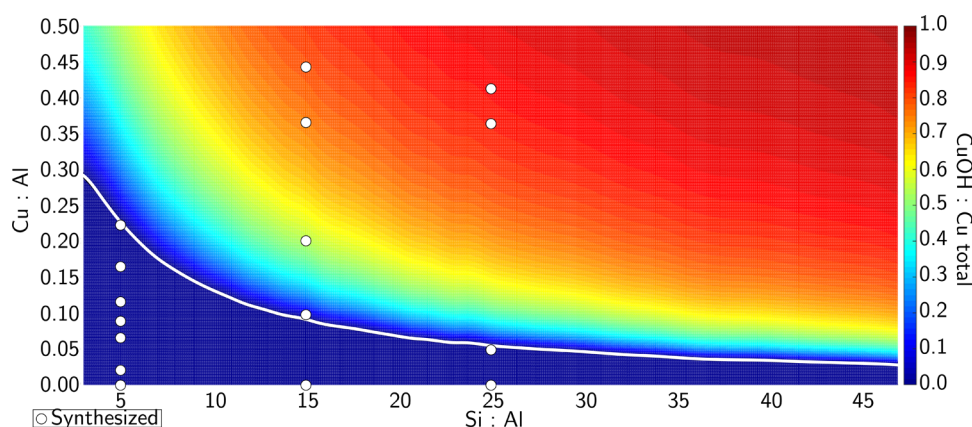
Figure 4. Predicted Cu site compositional phase diagram versus Si:Al and Cu:Al ratios. Color scale indicates predicted fraction of CuOH. White line demarcates transition from $[Z_2Cu^{II}]$-only region to mixed $[Z_2Cu^{II}]/[ZCu^{II}OH]$ region. White circles indicated compositions of synthesized Cu-SSZ-13 samples.

We generalize the analysis in Figure 2 to a range of temperatures and O_2 pressures at fixed H_2O partial pressure (2%) and plot the lowest free energy species at each set of conditions in Figure 3 in the form of a phase diagram. For reference, conditions 1 and 2 of Figure 2 are labeled with red boxes on Figure 3. The phase diagrams are insensitive to the H_2O pressure over the range of experimental interest. For comparison, we report the corresponding $T-P_{H_2O}$ diagram in Supporting Information 2.1.1-2. As discussed below, these diagrams indicate that the stable Cu state (CN, O_{fr} and oxidation state) depends sensitively on the environmental conditions over ranges of experimental interest and that the lowest free energy species differ for Cu complexes that charge compensate 1Al or 2Al sites.

2.1.2. 1Al and 2Al Cu Exchange Populations. To this point, we have treated the 1Al and 2Al sites independently. To place these two on a common energy scale, we computed the Cu exchange energy between the two sites:

$$[Z_2CuH_2O] + [ZH] \rightarrow [ZH]/[ZH] + [ZCuOH],$$
$$\Delta E = +66 \text{ kJ mol}^{-1} \qquad (6)$$
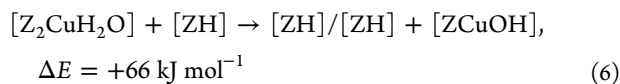
We evaluated this energy in a large supercell containing separated Z_2 and Z sites as well as in separate supercells constructed to conserve atomic numbers; results are in close agreement (+66 vs +69 kJ mol^{-1}), and structures are given in Supporting Information 2.1.2. We used the +66 kJ mol^{-1} result to offset the 0 K energies of $[Z_2Cu^{II}H_2O]$ and $[ZCu^{II}OH]$ and thus place the two site types on the same free energy y-axis shown in Figure 2. The zero of energy is defined as $[ZCu^I]$. The free energy associated with Cu near 2Al is substantially lower than that with Cu near 1Al at both 298 K (-142 kJ mol^{-1}) and 673 K (-55 kJ mol^{-1}). These results indicate that Cu ions prefer to segregate to 6MR 2Al exchange sites over a wide range of conditions.

The relative density of Cu ions in 6MR 2Al sites and in 8MR 1Al sites will depend on the total Cu content and the number of such 2Al and 1Al sites present in a given SSZ-13 sample. We determined the Al distribution as a function of Si:Al ratio by numerical simulation[17,66] assuming random Al distribution subject to Löwenstein's rule,[99] which prohibits 1NN Al pairs. We then assume that exchanged Cu ions populate all available 2NN and 3NN 2Al sites as $[Z_2Cu^{II}]$ before occupying 1Al sites as $[ZCu^{II}OH]$. Figure 4 reports the computed fraction of Cu

present as $[ZCu^{II}OH]$ as a function of Si:Al and Cu:Al ratios. The region below the white line corresponds to a composition space containing exclusively Cu species near 2Al, while the region above the white line contains gradually increasing $[ZCu^{II}OH]$ fractions that become the dominant species in the upper right red area. To ensure 2Al 6MR stays charge compensated by a single Cu past the saturation point, we computed the energy of two $[ZCu^{II}OH]$ in a 6MR (Supporting Information 2.1.2):

$$[Z_2CuH_2O] + [ZCuOH] \rightarrow [ZCuOH]/[ZCuOH]$$
$$+ [ZH], \qquad \Delta E = +81 \text{ kJ mol}^{-1} \qquad (7)$$
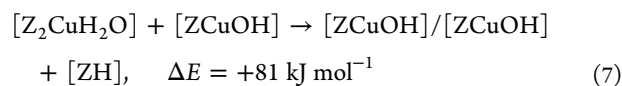
Thus, these 6MR 2Al sites will remain populated by $[Z_2Cu^{II}]$ as additional Cu is exchanged in the form of $[ZCu^{II}OH]$.

To test these model predictions, we prepared and analyzed a series of SSZ-13 catalysts of varying Si:Al and Cu:Al ratio (samples represented by white circles in Figure 4). An Al-rich SSZ-13 sample (Si:Al = 5) was synthesized using high Al FAU zeolite as the Al source[100] and characterized as reported previously,[28,66,83,101,102] while lower Al content SSZ-13 samples (Si:Al = 15, 25) were synthesized using Al(OH)$_3$ as the Al source.[69] Powder XRD patterns (Supporting Information 2.1.3-1) and Ar adsorption isotherms (87 K, Supporting Information 5.3-2) were consistent with the CHA topology on all H-form SSZ-13 samples. The number of H$^+$ sites on each H-SSZ-13 sample was quantified from the NH$_3$ evolved during TPD of NH$_4$-form samples, and were 0.65, 1.02, and 0.98 H$^+$:Al for the Si:Al ratios of 5, 15, and 25, respectively. The high Al H-SSZ-13 sample (Si:Al = 5) contained fewer H$^+$ sites than its number of framework Al atoms (H$^+$:Al$_f$ = 0.76),[102] reflecting the imprecision with which ex situ methods such as ^{27}Al MAS NMR spectroscopy may characterize structural surrogates for H$^+$ sites. It also reflects the nonuniformity of SSZ-13 samples prepared using FAU to CHA interconversion methods,[100] for which repeat synthesis experiments crystallized samples that contained H$^+$:Al ratios that varied between 0.45 and 0.85 (Supporting Information 2.1.3-4).

Increasing amounts of Cu were exchanged into these three (Si:Al = 5, 15, 25) H-SSZ-13 samples from aqueous-phase Cu^{II}(NO$_3$)$_2$. The number of residual H$^+$ sites was quantified using NH$_3$ TPD, which was performed after samples were saturated with gaseous NH$_3$ (433 K) and purged in wet helium

(3% H_2O, 433 K) to desorb Lewis acid-bound NH_3 and selectively retain NH_4^+ species,[101] as illustrated by eq 8:

$$Z_*CuNH_3 + H_2O \rightarrow Z_*CuH_2O + NH_3$$
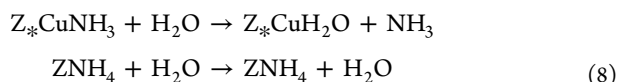
$$ZNH_4 + H_2O \rightarrow ZNH_4 + H_2O \qquad (8)$$

Figure 5 shows the number of residual H^+ sites present on each Cu-SSZ-13 sample after oxidative treatment in flowing air (773
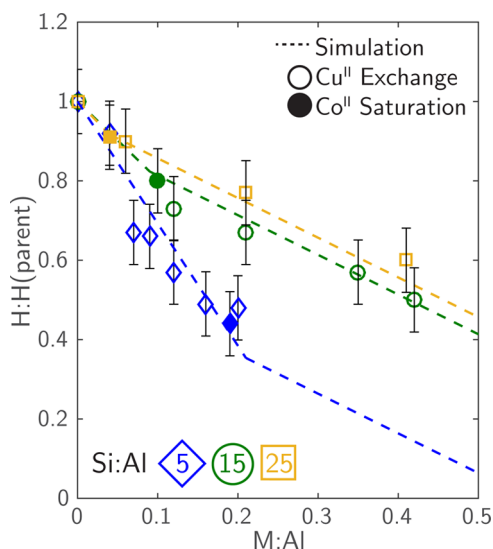

Figure 5. Residual H^+ sites per parent sample H^+ from NH_3 titrations on oxidized M-SSZ-13 samples versus extent of M/Al exchange for Si:Al = 5 (blue ◇), 15 (green ○), and 25 (orange □). Open and filled symbols denote Cu^{2+} and saturated Co^{2+} exchange, respectively. Dashed lines are model predictions.

K), normalized by the number of H^+ sites quantified on their respective H-SSZ-13 parent samples after the same oxidative treatment, as a function of Cu:Al ratio. The dashed lines in Figure 5 represent the number of residual H^+ sites as a function of Cu:Al ratio predicted from the simulation results in Figure 4. At a Si:Al ratio of 5, each exchanged Cu cation decreased the number of residual H^+ sites by two (on average) up to a Cu:Al ratio of 0.20 (Figure 5),[101,102] consistent with the exchange stoichiometry:

$$Z_2H_2 + Cu^{II} \rightarrow Z_2Cu^{II} + 2H^+ \qquad (9)$$
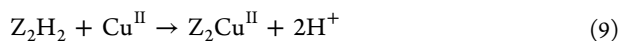
On samples with Si:Al ratios of 15 and 25, each exchanged Cu exchanged two H^+ sites until Cu:Al ratios of 0.10 and 0.04, respectively, but only one additional H^+ site beyond this limit (Figure 5), consistent with the exchange reaction:

$$ZH + Cu^{II}H_2O \rightarrow ZCuOH + 2H^+ \qquad (10)$$
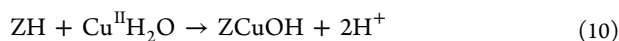
These Cu:H^+ exchange stoichiometries provide experimental evidence that cationic Cu species exchange sequentially as $[Z_2Cu^{II}]$ sites until saturation and then as $[ZCu^{II}OH]$ sites (Figure 2).

Figure 6 shows FTIR quantification of the disappearance of Brønsted ZH species and the appearance of $[ZCu^{II}OH]$ as a function of Cu density on the series of Cu-SSZ-13 samples with Si:Al = 15. The H-SSZ-13 spectrum includes four features in the O−H region, including modes at 3605 and 3580 cm^{-1}[103,104] from Brønsted sites, at 3732 cm^{-1} from isolated silanols, and at 3700 cm^{-1} from vicinal silanols.[105] The integrated area of the Brønsted ZH peaks of the Cu:Al 0.12
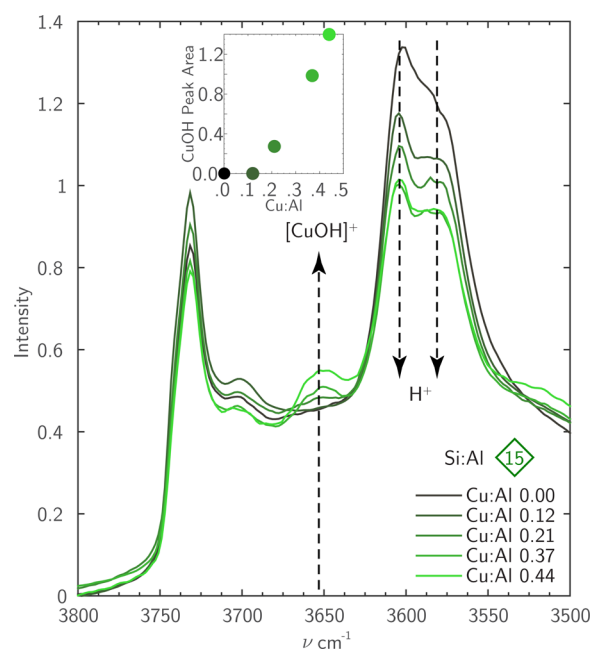

Figure 6. FTIR spectra of oxidized Cu-SSZ-13 samples (Cu:Al = 0−0.44, Si:Al = 15). Inset: Integrated 3660 cm^{-1} CuO−H area as a function of Cu:Al ratio.

sample, taking that of the H-SSZ-13 sample as the baseline, decreased with a 2:1 H^+:Cu ratio (Supporting Information 2.1.3-3), consistent with eq 9. A new, fifth feature appears at 3660 cm^{-1} in Cu:Al > 0.21 samples, at a location consistent with previous assignment to[64] and the computed harmonic O−H stretch frequency of $[ZCu^{II}OH]$. The integrated area of this 3660 cm^{-1} band increases linearly across the range Cu:Al = 0.21−0.44 (Figure 6, inset), and the integrated areas of the Brønsted OH stretches decrease concurrently in a 1:1 H^+:Cu ratio, consistent with eq 10. These vibrational data provide strong additional support for the sequential population of $[Z_2Cu^{II}]$ followed by $[ZCu^{II}OH]$ sites.

Co^{II} exchange provides a third independent enumeration of the number of 2Al 6MR sites on each sample, because Co^{II} does not exchange at single Al sites as $[ZCo^{II}OH]$ at the exchange pH used here (pH ≈ 3.2).[106] Samples with Si:Al ratios 5, 15, and 25 were saturated with Co^{II}, and the Co:Al contents were determined by atomic absorption (Supporting Information 2.1.3-2) to be 0.19, 0.10, and 0.04, respectively. These values agree quantitatively with the maximum number of 2Al 6MR sites predicted for each Si:Al ratio in Figure 4 for a random Al distribution in SSZ-13. Furthermore, the numbers of residual of H^+ sites on Co-saturated SSZ-13 samples were quantified by NH_3 titration and are plotted on Figure 5 as filled symbols, and agree quantitatively with the transition Cu:Al ratios between exchange of $[Z_2Cu^{II}]$ and $[ZCu^{II}OH]$ species. These results indicate that isolated Co^{II} and Cu^{II} exhibit identical preferences for 2Al 6MR sites and that both cations replace two Brønsted sites via eq 9 when exchanged at these sites.

The Cu:Al values that demarcate the transition between formation of $[Z_2Cu^{II}]$ sites and $[ZCu^{II}OH]$ sites are 0.20, 0.10, and 0.04 for the H-SSZ-13 samples with Si:Al ratios of 5, 15, and 25, respectively (Figure 5). These Cu:Al values are identical, within error, to the fraction of 2Al 6MR sites predicted from simulation of Al distribution in CHA frameworks at these Si:Al ratios (Figure 4). Taken together, these
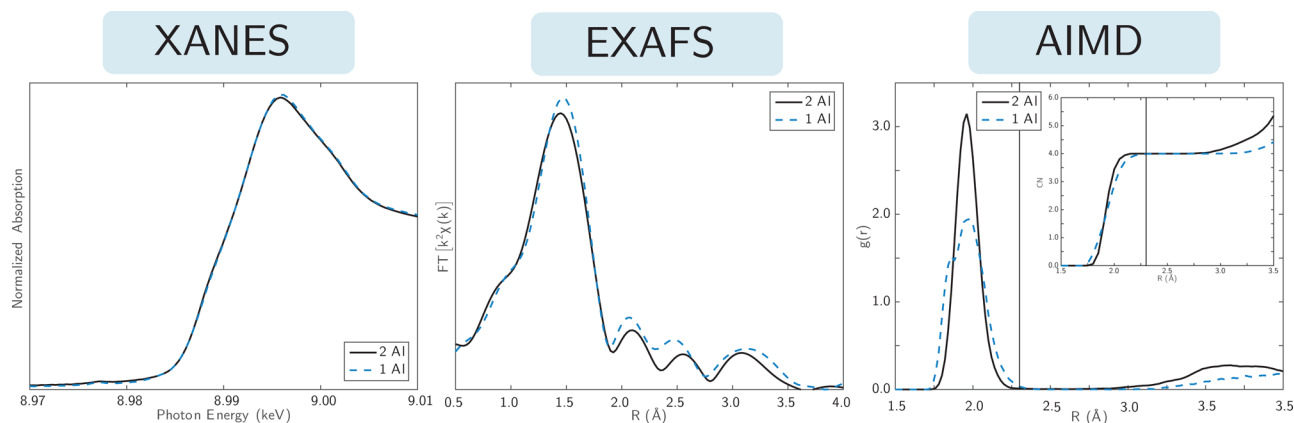
Figure 7. Left: XANES spectra collected on the 1Al (teal dashes) and 2Al (black lines) Cu-SSZ-13 samples under treatment in 2% H_2O, 20% O_2 at 298 K. Middle: EXAFS spectra under the same conditions. Right: 298 K AIMD RDFs and integrated RDFs (inset).
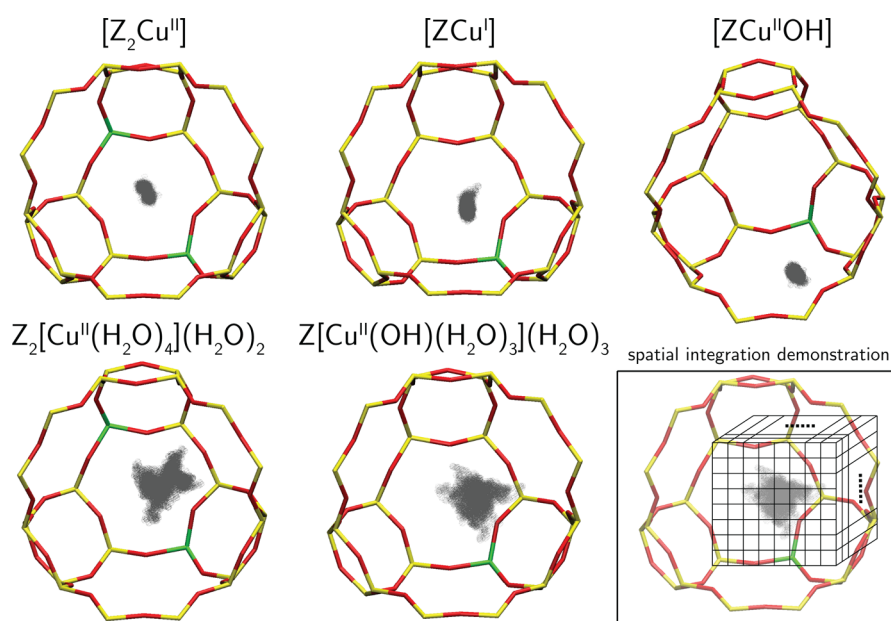

Figure 8. Cu positions (gray balls) visited during 90 ps of NVT AIMD at 298 K. Fixed zeolite framework shown for ease of visualization; framework was unconstrained during dynamics. Inset illustrates discretization used to compute relative Cu mobilities.

experimental and computational findings indicate that under the conditions of synthesis applied here,[107] the concentration of 2Al 6MR sites is in agreement with a random Al distribution in SSZ-13 subject to Löwenstein's rule, that 2Al 6MR are the preferred sites for Cu^{II} exchange, and that these sites saturate before remaining 1Al sites are populated with $[ZCu^{II}OH]$. This quantification allows us to identify and contrast the structures, properties, and catalytic performance under low-temperature (473 K) standard SCR conditions of samples that contain predominantly $[Z_2Cu^{II}]$ or $[ZCu^{II}OH]$ sites. We choose a sample with Si:Al = 5 and Cu:Al = 0.08 to represent a $[Z_2Cu^{II}]$ site and a sample with Si:Al = 15 and Cu:Al = 0.44, similar in composition to that explored by others,[64,71,73] to represent $[ZCu^{II}OH]$. We refer to these as the "2Al" and "1Al" samples, respectively. While the 1Al sample contains ~20% $[Z_2Cu^{II}]$ sites, they are in the minority, and the bulk spectroscopic techniques applied here are primarily sensitive to the majority $[ZCu^{II}OH]$ site.

2.2. Copper Cation Structure under Ex Situ Conditions. We next combined XAS and AIMD simulations to explore the molecular and electronic structures of both model

1Al and 2Al samples as a function of the conditions represented in Figure 3. Results are summarized in Figures 7 and 8 and in Table 2. We expect the framework composition to be robust to the conditions studied here. Significant dealumination of SSZ-13 is observed only after several hours of exposure to 10% H_2O at ~1000 K.[60,79,108,109]

2.2.1. Condition 1: Ambient Atmosphere (XAS/AIMD). First, both 1Al and 2Al samples were subjected to high-temperature oxidative treatments and then exposed to ambient atmosphere at 298 K, corresponding to condition 1 of Figure 3. The Cu K-edge X-ray absorption near edge spectra (XANES) collected on both samples were indistinguishable, as shown in Figure 7, left. A single edge at 8.988 keV corresponds to the 1s → 4p transitions of a Cu^{II} ion in a distorted square-planar or octahedral coordination.[82] EXAFS spectra of both samples from the same energy scan (Figure 7, middle) exhibited a high intensity first coordination shell peak at ~1.5 Å. The spectra were fitted using a $Cu_2O(s)$ experimental reference to estimate 4.0 Cu−O bonds (1.94 Å average distance) and 4.2 Cu−O bonds (1.93 Å average distance), respectively, on the 2Al and 1Al samples, which are identical within the ±5% error of the fit

Table 2. Comparison of AIMD (Left) and EXAFS (Right) Characterization of 2Al and 1Al Sites, Including Cu–X (X = O, N) Coordination Number (CN), Average Cu–X Distances, and Whether Second-Shell Features Appear

gas condition	sample	CN	avg. bond dist.	second shell	Cu mobility[c]
		AIMD | EXAFS			
condition 1 (ambient)	1Al	4.0|4.2	1.96|1.93	N|N	1.38
	2Al	4.0|4.0	1.96|1.94	N|N	1.00
condition 2 (O$_2$)	1Al	3.0|3.0	1.89|1.91	Y|Y	0.11
	2Al	3.9|3.8	2.02|1.94	Y|Y	0.14
condition 3 (He)	1Al	2.5[a]|2.4	1.92[a]|1.92	Y|Y	0.14[a]
	2Al	3.7[a]|3.6	2.50[a]|2.40	Y|Y	0.14[a]
NO + NH$_3$, 473 K	1Al	2.0|2.2	1.89|1.88	N|N	3.26
	2Al	2.0|2.1	1.89|1.88	N|N	1.83
O$_2$ + NH$_3$, 473 K	1Al	3.3[b]|3.2	1.97[b]|1.92	N|N	2.21[b]
	2Al	3.6[b]|3.5	2.00[b]|1.92	N|N	1.31[b]

[a]XANES weighted average of Cu^I (ZCu^I) and Cu^{II} (Z$_2$Cu and ZCuOH) structures obtained from AIMD. [b]XANES weighted average of Cu^I (ZCu^I(NH$_3$)$_2$ and ZNH$_4$/ZCu^I(NH$_3$)$_2$) and Cu^{II} (Z$_2$Cu(NH$_3$)$_4$ and ZCu(OH)(NH$_3$)$_3$) structures obtained from AIMD. [c]Volume visited by the minimum free energy forms of Cu^I and Cu^{II} (Figure 3) during 90 ps AIMD, normalized to the volume of hydrated Z$_2$Cu (1.00).

(details in Supporting Information 2.2.1-1). Higher coordination shells beyond 2.0 Å appear with low intensity on both samples and indicate Cu–O bonds with extra-framework O species, as evidenced by the absence of scattering from Si or Al atoms bound to O$_f$. The XANES and EXAFS spectra are indistinguishable from each other and that of aqueous Cu^{II} complexes,[82] which are also known to form a square-planar tetraaquo complex. These observations are in agreement with the phase diagram condition 1 predictions shown in Figure 3.

The EXAFS provides an ensemble average of the Cu coordination environment. To extract comparable information from simulation, we performed 298 K AIMD simulations (60 ps of equilibration followed by 90 ps of sampling) on the lowest free energy hydrated forms of [Z$_2$Cu^{II}] and [ZCu^{II}OH]. In both cases, Cu remained near the center of the cage (Figure 1C) and was dynamic. Figure 8 superimposes the Cu positions relative to the zeolite cage during the 90 ps sampling. To quantify Cu mobility, we discretized the supercell into 0.2 × 0.2 × 0.2 Å cubes, counted the cubes visited at least once during the simulation, scaled by the cube volume, and normalized to the volume visited by Z$_2$[Cu^{II}(H$_2$O)$_4$](H$_2$O)$_2$. Results are summarized in Table 2 and further detailed in Supporting Information 2.2.1-2. Z[Cu^{II}OH(H$_2$O)$_3$](H$_2$O)$_3$ is estimated to be 1.38 times as mobile as [Z$_2$Cu^{II}(H$_2$O)$_4$](H$_2$O)$_2$, consistent with the weaker electrostatic attraction to a single Al as compared to two proximal Al atoms. Throughout the Z[Cu^{II}OH(H$_2$O)$_3$](H$_2$O)$_3$ simulation, H atoms are observed to hop between nonframework O with a barrier of ~20 kJ mol^{-1}, causing O bound to Cu to spend time as both OH and H$_2$O.

The right panel of Figure 7 shows the computed radial distribution functions (RDFs) between Cu and all heavy atoms. Both RDFs show a prominent peak near 2 Å corresponding to the first coordination shell with peak area corresponding to four O atoms. These first RDF peaks correspond with the first EXAFS peak (the RDF and EXAFS are offset due to the difference between electron scattering and interatomic distances). The 1Al RDF is broadened in comparison to the 2Al due to the presence of both shorter Cu–OH and longer Cu–H$_2$O bonds that are not resolvable by EXAFS. The RDFs are near-zero between 2.2 and 3.0 Å; structure appears beyond
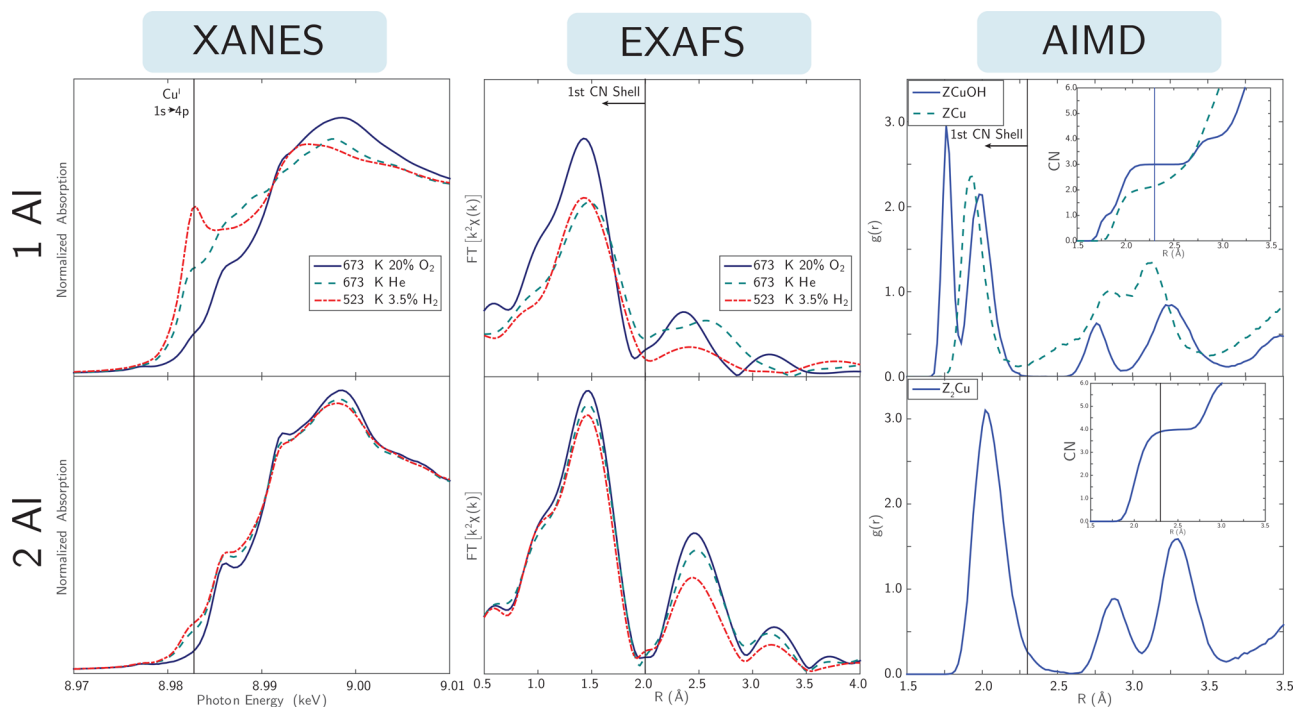

Figure 9. Left: XANES spectra collected on the 1Al (top) and 2Al (bottom) samples after treatment in 20% O$_2$ at 673 K (solid blue lines), He at 673 K (dashed teal lines), and in 3% H$_2$ at 523 K (dot–dash red lines). Middle: Corresponding EXAFS spectra. Right: AIMD Cu–Si/O/Al RDFs for ZCuOH and ZCu (top) and Z$_2$Cu (bottom). Insets show integrated RDFs.

Table 3. Characterization of 2Al and 1Al Cu-SSZ-13 Catalysts during Low-Temperature (473 K) Standard SCR: XANES Cu^{I}/Cu^{II} Fraction, SCR Rates (per Cu and mol NO) in the Operando Reactor/Plug-Flow Reactor, Apparent Activation Energies, and Apparent NO, O$_2$, and NH$_3$ Orders

	Cu^{I}|Cu^{II}	TOR^a	E_{app} (kJ mol^{-1})	NO order	O$_2$ order	NH$_3$ order
2Al	50|50 ± 5	8.3/7.3	60 ± 10	0.8/0.8	0.3/0.3	−0.2/−0.1
1Al	55|45 ± 5	9.9/8.0	74 ± 10	n.m./0.7^b	n.m./0.3^b	n.m./0.0^b

^{a}(s^{-1} mol Cu^{1-} mol NO^{-1}) × 10^{-3}. ^{b}n.m. = not measured; 1Al orders were measured only in the PFR.
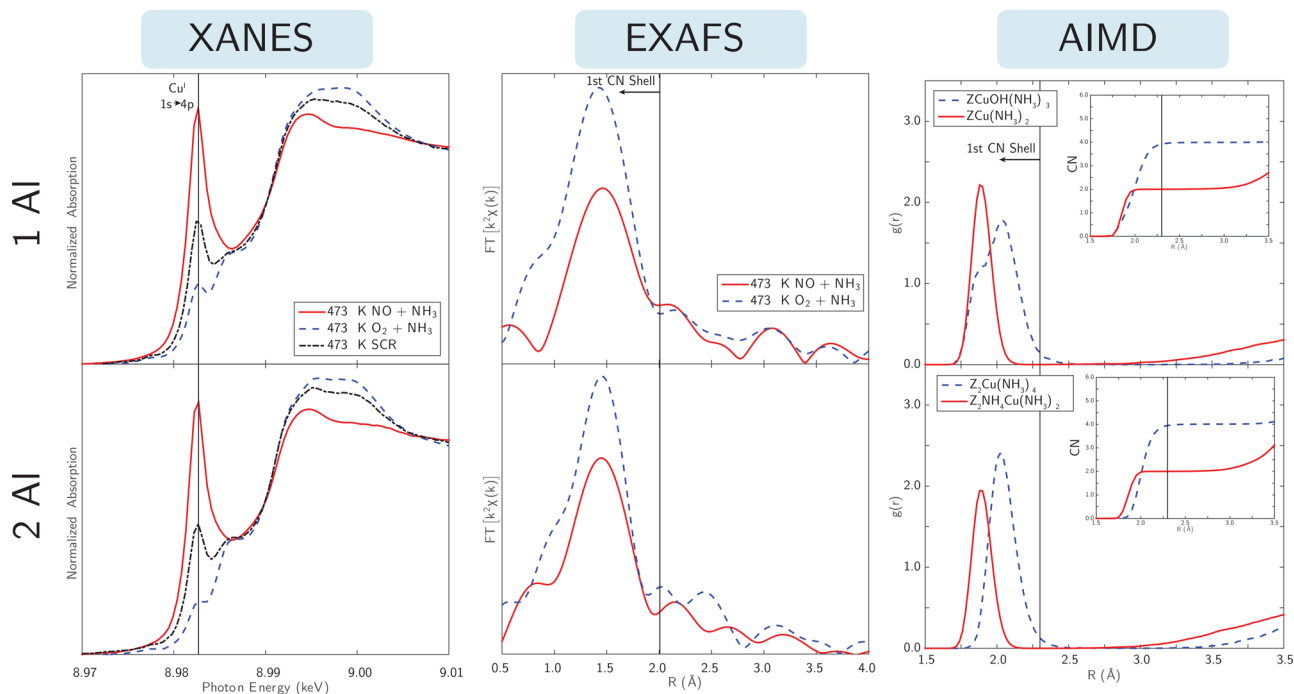

Figure 10. Left: XANES spectra of the 1 Al (top) and 2Al (bottom) Cu-SSZ-13 samples under treatment in 2% H$_2$O, 10% O$_2$, 300 ppm of NH$_3$ at 473 K (O$_2$ + NH$_3$, blue traces), 2% H$_2$O and 300 ppm of NO/NH$_3$ at 473 K (NO + NH$_3$, red lines), and in 2% H$_2$O, 10% O$_2$, 300 ppm of NO/NH$_3$ at 473 K (black traces). Middle: EXAFS collected under same conditions. Right: AIMD Cu–Si/O/Al RDFs for the most stable Cu^{I} (red lines) and Cu^{II} (blue traces) species on the 1 and 2Al sites in the presence of NH$_3$. Insets: Integrated RDFs.

3.0 Å. The results are consistent with the observation of only low intensity peaks beyond the first major one in the EXAFS and H$_2$O solvated Cu complexes.

2.2.2. Condition 2: 20% O$_2$, 673 K (XAS/AIMD). Next, we collected XANES spectra at 298 K on both samples after 1 h treatment at 673 K in O$_2$, corresponding to condition 2 in Figure 3. The vessels were sealed before cooling to prevent rehydration of Cu. Resultant XANES and EXAFS are shown in Figure 9. In addition to the 8.988 keV Cu^{II} edge feature observed in Figure 7, an additional feature appears at 8.987 keV that reflects Cu^{II} present in a lower than octahedral coordination environment.[20] Further, on the 1Al sample, a low intensity peak appears at 8.983 keV that we assign to 5% Cu^{I} based on a fit using Cu^{I} and Cu^{II} references (Supporting Information 2.2.2-1).

The EXAFS (Figure 9, middle) exhibit high intensity peaks at ∼1.5 Å that fit to 3.0 Cu–O bonds at 1.91 Å and to 3.8 Cu–O bonds at 1.94 Å on the 1Al and 2Al samples, respectively (Table 2). Consistent with the higher first-shell coordination and closer proximity to multiple Si/Al, the 2Al sample also exhibits a more distinct second shell peak at ∼2.4 Å than that on the 1Al sample. To ensure reversibility, we cycled samples between condition 1 and condition 2 and confirmed that XAS spectra were identical to those shown in Figure 7.

These EXAFS features are consistent with those expected for the [Z$_2$Cu^{II}] and [ZCu^{II}OH] species predicted to predominate at condition 2. Cu remains bound to multiple O$_f$ for the duration of AIMD simulations on each, and each are computed to be about 8 times less mobile than the Z$_2$[Cu^{II}(H$_2$O)$_4$]-(H$_2$O)$_2$ reference. The [Z$_2$Cu^{II}] site oscillates between three nearly isoenergetic minima (Supporting Information 2.2.2-2) that differ in the O$_f$ nearest-neighbor to Cu. The first shell in the RDF (Figure 9, bottom right) convolutes these three and integrates to a CN 3.9. By deconvolution of the RDF, we assign the second feature at ∼2.8 Å to one Al and one Si atom nearest Cu (Supporting Information 2.2.2-3). The AIMD CN is consistent with the EXAFS fit.

In contrast, [ZCu^{II}OH] only exhibits a "wagging" into and out of the 8MR plane during AIMD. The Cu–O$_f$ and Cu–OH pairs appear as sharp features in the RDF (Figure 9, top right). The integrated RDF and fitted CN are identical. The slightly broad second shell feature at ∼2.75 Å arises from the Al nearest Cu (Figure 1B). This second shell feature is at 0.25 Å shorter distance and one-half the integrated area of the [Z$_2$Cu^{II}] second shell, consistent with both the location and the magnitude of the EXAFS second shell features.

2.2.3. Condition 3: He, 673 K (XAS/AIMD). As noted above, a small amount of Cu^{I} appears in the XANES of the calcined 1Al sample. This autoreduction feature[64,71] becomes more

prominent after treating the 1Al sample in flowing helium at 673 K for 1 h following the calcining treatment (Figure 9, left panel). From spectral deconvolution and EXAFS fitting, we infer 55% of the Cu to be present as Cu^I and the mean Cu−O coordination number to decrease to 2.4 (Table 2). In contrast, only 10% Cu^I is observed on the 2Al sample following the same He treatment, and the coordination number is unchanged. The Cu^I feature becomes even more pronounced and the Cu^I fraction increases to 65% on the 1Al samples treated in 3% H_2 at 523 K;[76,77] the 2Al sample is changed negligibly by H_2 reduction. These observations of autoreduction in the 1Al but not 2Al samples are consistent with the predictions for condition 3 in Figure 3. That reduction is not complete on the 1Al sample suggests some kinetic as well as thermodynamic contribution to the autoreduction process, possibly associated with the mobility of the $[ZCu^{II}OH]$. Reoxidation of samples after the He purge or H_2 treatment returns the XANES and EXAFS spectra to their postcalcination forms (additional details in Supporting Information 2.2.3-1), indicating that reduction and reoxidation are reversible.

To interpret the observed EXAFS, we used 298 K AIMD to compute the dynamics of the reduced $[ZCu^I]$ site. The Cu ion stays within the 6MR and retains coordination to the same two O_f atoms; the computed RDF (Figure 9) is dominated by a Cu−O_f feature at 1.93 Å that integrates to CN 2.1. The Cu mobility is enhanced by about 20% as compared to $[ZCu^{II}OH]$ and $[Z_2Cu^{II}]$, but still roughly 8 times less than hydrated $[Z_2Cu^{II}]$. The second shell feature in EXAFS, spanning from roughly 2−3 Å, is echoed in the broad AIMD RDF past the first coordination shell, a consequence of $[ZCu^I]$ mobility within the 6MR.

2.3. Copper Speciation at SCR Conditions. The ex situ characterizations above show that Cu cations in the 1Al and 2Al samples are identical under ambient and hydrated conditions, exhibit different coordination after high-temperature oxidation, and respond differently to high-temperature reduction. We next explore the implications under catalytic conditions relevant to low-temperature NO_x SCR.

2.3.1. Operando XAS Spectra and SCR Kinetics. We used a custom-built reactor[110] designed to collect XAS spectra in operando to determine the Cu oxidation states of the 2Al and 1Al samples during steady-state SCR (300 ppm of NO, 300 ppm of NH_3, 10% O_2, 2% H_2O) at 473 K under differential and plug-flow conditions (<20% NO conversion). Observed SCR turnover rates (TOR, mol NO s^{-1} mol Cu^{-1}), apparent NO, O_2, and NH_3 reaction orders, and apparent activation energies (E_{app}) (Table 3) were identical on the 2Al and 1Al samples, within experimental error, and identical to values measured on these samples in a different plug-flow reactor (section 5.5). Operando XANES spectra for the two samples (Figure 10, left, black traces) indicate the presence of 50% and 55% Cu^I (8.983 keV peak), respectively, that are identical within the fitting error (5%). Although the presence of both Cu^{II} and Cu^I species during standard SCR redox cycles is not surprising,[53,73,83,84,95] the identical Cu^I fractions and kinetic parameters (Table 3) are unexpected given the different structures, dynamics, and reducibility of $[Z_2Cu^{II}]$ and $[ZCu^{II}OH]$ species in He and H_2. These operando characterization results suggest that cationic copper sites are functionally equivalent during low-temperature standard SCR at 473 K.

2.3.2. SCR Gas Species Binding Energies. To understand Cu coordination in the SCR gas mixture (H_2O, N_2, NH_3, NO, O_2), we first computed adsorption energies of these species as well

as NO_2, which is often proposed as an SCR intermediate,[73,91−94] on the oxidized and reduced forms of the 1Al and 2Al Cu sites using the same AIMD and HSE06-TSvdw optimization protocol. The computed NH_3 binding energy to the $[ZH]/[ZCu^I]$ Brønsted site is −151 kJ mol^{-1}, quantitatively consistent with NH_3 differential heats observed via microcalorimetry on zeolitic H^+ sites:[111−115]

$$[ZH]/[ZCu^I] + NH_3 \rightarrow [ZNH_4]/[ZCu^I] \qquad (11)$$

Thus, the NH_4^+ form of this site prevails under SCR conditions, and we used the $[ZNH_4]/[ZCu^I]$ structure shown in Figure 11 as the model for a reduced 2Al site.
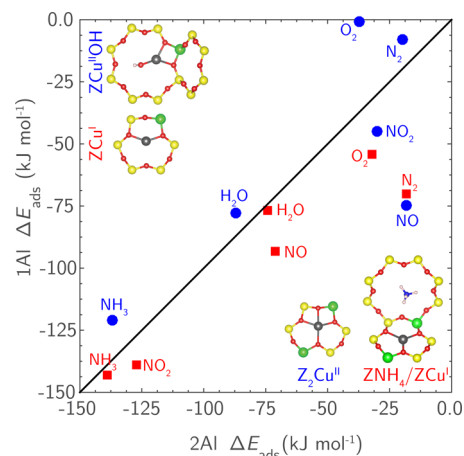

Figure 11. Parity plot of HSE06-TSvdw-computed binding energies of gaseous species relevant to SCR on 2Al oxidized (Z_2Cu, blue) and reduced (ZNH_4/ZCu, red) versus corresponding oxidized (ZCuOH, blue) and reduced (ZCu, red) 1Al sites.

Computed 1Al site binding energies are plotted against 2Al sites in Figure 11. Binding energies without the TSvdw correction are approximately 20 kJ mol^{-1} more positive. Binding energies (Supporting Information 2.3.2-1) and structures on the $[Z_2Cu^{II}]$ and $[ZCu^{II}OH]$ sites are generally consistent with those for H_2O, NO, and NH_3 reported elsewhere,[67,73,86−88] although the inclusion of hybrid exchange significantly decreases the NO binding relative to the GGA values.[67,83,86−88] The 1Al and 2Al binding energies are roughly linearly correlated, although deviations as large as 50 kJ mol^{-1} are evident. O_2 interacts weakly with all sites; H_2O and NO exhibit intermediate binding strengths. NH_3 binds by −120 to −140 kJ mol^{-1} on all four Cu adsorption sites and does not significantly alter the Cu oxidation state. NO_2 binds strongly to reduced sites (oxidizing the Cu center to form a nitrite) but interacts weakly with oxidized Cu. NO is a notable outlier from the linear correlation: the HSE calculations predict NO to bind weakly to $[Z_2Cu^{II}]$ (−25 kJ mol^{-1}) but with intermediate strengths on $[ZCu^{II}OH]$ (−75 kJ mol^{-1}). NO locates near the OH ligand rather than Cu, similar to structures for this species reported elsewhere,[67] but does not form a HONO-like structure. N_2 more strongly adsorbs to $[ZCu^I]$ than to other sites.

Because NH_3 out-binds all other species and is similar in its coordination behavior to H_2O, we explored the sequential binding of additional NH_3 on all four sites:

$$*(NH_3)_{x-1} + NH_3 \xrightarrow{\Delta E_{ads}} *(NH_3)_x \qquad (12)$$
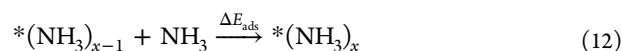
using an AIMD anneal at 473 K followed by HSE06-TSvdw optimization. Results are summarized in Table 4; structures and

Table 4. HSE06-TSvdw-Computed Sequential NH$_3$ Adsorption Structures and Energies[a]

	+xNH$_3$	1	2	3	4
[Z$_2$Cu^{II}]	ΔE_{ads} (kJ mol^{-1})	−132	−136	−123	−132
	cage location	A	A	B	C
	O$_f$/total CN	3/4	2/4	1/4	0/4
[ZNH$_4$]/[ZCu^{I}]	ΔE_{ads} (kJ mol^{-1})	−134	−150	−72	−73
	cage location	B	C	C	C
	O$_f$/total CN	1/2	0/2	0/2	0/2
[ZCu^{II}OH]	ΔE_{ads} (kJ mol^{-1})	−117	−119	−116	−47
	cage location	B	C, B[b]	C	C
	O$_f$/total CN	2/4	0/3, 1/4[b]	0/4	0/4
[ZCu^{I}]	ΔE_{ads} (kJ mol^{-1})	−137	−151	−75	−41
	cage location	B	C	C	C
	O$_f$/total CN	1/2	0/2	0/2	0/2

[a]Cage location indicates optimized ion location referenced to Figure 1. CN and O$_f$ indicate total Cu coordination number and number of close framework O contacts, respectively. [b]Trigonal planar, square planar values.

normalized Cu Bader charges are detailed in Supporting Information 2.1.1-1. Binding energies are roughly constant as NH$_3$ displaces O$_f$ from the Cu coordination sphere. Cu^{I} and Cu^{II} retain 2-fold and 4-fold coordination, respectively; additional NH$_3$ beyond these limits are more weakly bound and not directly associated with Cu, instead forming hydrogen bonds with NH$_3$ in the first coordination sphere. The only exception is ZCu^{II}OH(NH$_3$)$_2$; this species adopts a square-planar conformation including a single O$_f$ ligand at 0 K, but in the finite T dynamics adopts a trigonal planar form, free from

O$_f$, for ~90% of the trajectory. Energy and entropy are evidently closely balanced between the two configurations.

2.3.3. NH$_3$ Phase Diagrams. We used a first-principles thermodynamic analysis to rank the free energies of the NH$_3$ species in Table 4 and H$_x$O$_y$ structures from Figure 2, 42 species in total, taking O$_2$, H$_2$O, and NH$_3$ as oxygen, hydrogen, and nitrogen references, respectively:

$$Z_*Cu + \frac{x}{2}\left(H_2O - \frac{1}{2}O_2\right) + \frac{y}{2}O_2$$
$$+ z\left(NH_3 - \frac{3}{2}H_2O + \frac{3}{4}O_2\right) \xrightarrow{\Delta G_{form}} Z_*CuH_xO_yN_z$$
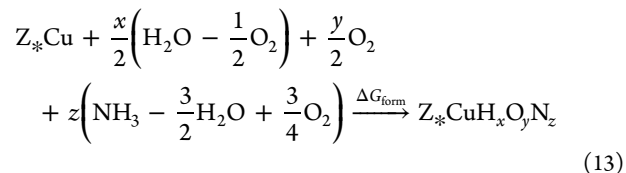
$$(13)$$

Figure 12 reports the lowest free energy 1Al and 2Al species as a function of T and O$_2$ partial pressure at H$_2$O and NH$_3$ concentrations of 2%, and 300 ppm, respectively, representative of the experimental conditions shown in Figure 10. We chose O$_2$ pressure as an independent variable for direct comparison to the experimental results detailed in the proceeding section. The resultant phase diagrams are substantially different from the H$_x$O$_y$ ones in Figure 3; NH$_3$-containing species dominate the diagrams up to 773 K, and H$_2$O is an unimportant adsorbate. The most prominent species in the 1Al and 2Al diagrams are reduced Cu^{I} species and oxidized Cu^{II} species, respectively, although both oxidized and reduced forms of Cu appear on both diagrams. Both sites are saturated with NH$_3$ at 473 K and successively lose NH$_3$ ligands with increasing temperature. At 473 K, the 2Al phase diagram (Figure 12, right) shows Cu preferring Cu^{I}(NH$_3$)$_2$ as the O$_2$ concentration decreases, and Cu^{II}(NH$_3$)$_4$ species as the O$_2$ concentration increases. The Cu^{I}(NH$_3$)$_2$ complex is the most stable 1 Al species over the entire O$_2$ range examined here.

Sidebars in Figure 12 rank the relative free energies of intermediates at the condition indicated by the chrome spheres
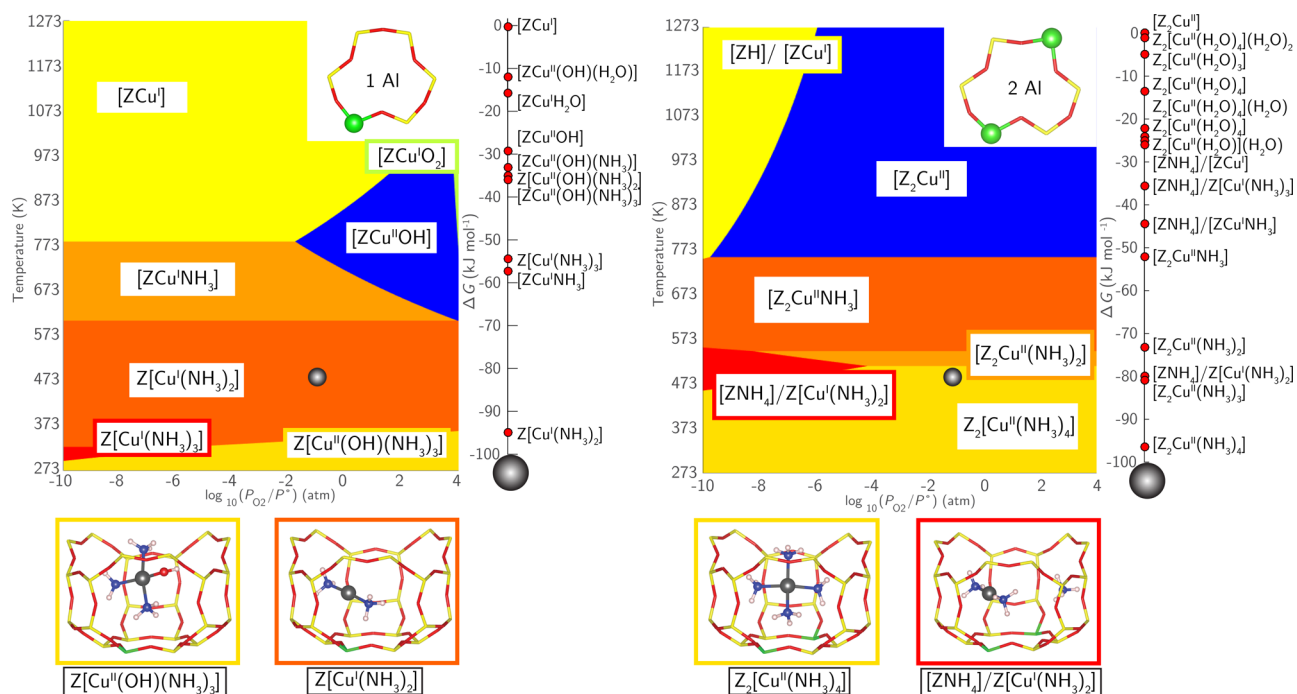

Figure 12. Phase diagrams for 1Al (left) and 2Al (right) sites with varying T and P_{O2} at 300 ppm of NH$_3$ and 2% H$_2$O. Relative rankings for all species $\Delta G_{form} < 0$ at 473 K and 10% O$_2$ (chrome spheres on the phase diagrams) are given to the right of each phase diagram. The structures shown on the bottom are the most stable Cu^{I} (red) and Cu^{II} (golden) under these conditions.

in the phase diagrams (473 K and 10% O_2), equivalent to those in Figure 10. Species with $\Delta G_{form} > 0$ kJ mol^{-1} are excluded for clarity; full results are tabulated in Supporting Information 2.3.4-1. The analysis predicts a reduced and NH_3-saturated Cu^I to be the most stable 1Al species at these conditions. Cu^I complexes with one or three NH_3 ligands are higher in free energy, and the first Cu^{II} species to appear is $Z[Cu^{II}OH-(NH_3)_3]$ at 50 kJ mol^{-1} higher free energy than the most stable species. Thus, these two NH_3-saturated and O_f-liberated complexes are the most likely dominant forms of Cu^I and Cu^{II} under SCR conditions in the 1Al catalyst. The Cu^I/Cu^{II} ordering is reversed at the 2Al site, where the most stable complex is an oxidized and NH_3-saturated $Z_2[Cu^{II}(NH_3)_4]$ at 16 kJ mol^{-1} below the reduced and NH_3-saturated $[ZNH_4]/$ $Z[Cu^I(NH_3)_2]$. The Cu^I/Cu^{II} fractions are the same in the operando XANES (Figure 10) on the 1Al and 2Al samples and likely kinetically rather than thermodynamically controlled. The thermodynamic screening identifies the species most relevant to catalysis and highlights the importance of NH_3 coordination under SCR conditions.

2.3.4. XAS/AIMD for Cu^I/Cu^{II} with NH_3. To explore Cu structure and dynamics under SCR conditions, we collected XAS and AIMD information on both 1Al and 2Al samples prepared with subsets of SCR gas mixtures that place them primarily in the Cu^I and Cu^{II} states.

Figure 10 shows the XANES and EXAFS at 473 K of 1Al and 2Al samples treated in 300 ppm of NO and NH_3. Consistent with previous reports,[73,83,95] this treatment reduces Cu. In fact, the XANES and the EXAFS on both samples are indistinguishable, and the XANES fit to a Cu^I fraction of 100%. A prominent first shell peak at 1.88 Å in the EXAFS fits to 2.1 CN, which EXAFS cannot distinguish between O and N. The EXAFS is absent of longer-range structure.

These XAS results are consistent with the reduced Cu forms highlighted in Figure 12. We performed 473 K AIMD simulations on $[ZNH_4]/Z[Cu^I(NH_3)_2]$ and $Z[Cu^I(NH_3)_2]$ for the 2Al and 1Al sites, respectively. The linear $Cu^I(NH_3)_2$ species are identical in structure and, as evidenced in the dynamics trajectory (Figure 13) and the volume visited (Table 2), highly mobile. Computed RDFs between Cu and other heavy atoms are shown in Figure 10. As in the EXAFS, the lone
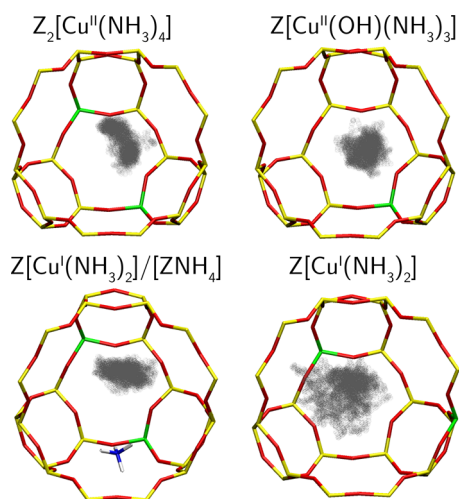
peak at 1.89 Å integrates to 2.0 CN; the Cu location is completely disordered with respect to the zeolite lattice. To probe the ability of this NH_3-mobilized Cu^I to diffuse between cages, we used the climbing image nudged elastic band (CI-NEB, Supporting Information 2.3.5-1) method to compute the energy to thread a $Cu^I(NH_3)_2$ ion through the 8MR. The path starts with one NH_3 in the plane of the 8MR, passes over a 37 kJ mol^{-1} transition state in which the Cu is centered within the ring, and ends with the other NH_3 in the 8MR. This modest barrier suggests rather facile transport of reduced Cu within the SSZ-13 lattice, as has been inferred from the NH_3-facilitated exchange of Cu^I.[116]

Figure 10 similarly shows XAS spectra collected on the same samples during exposure to an oxidizing mixture of NH_3 (300 ppm) and O_2 (10%) at 473 K. The XANES are again similar to one another but markedly different from those at the reducing condition. Both samples exhibit a peak at 8.983 keV corresponding to a Cu^I species, 27% and 17% on the 1Al and 2Al samples, respectively, and a balance of Cu^{II} species. EXAFS shows prominent first coordination shells at 1.5 Å that fit to 3.2 and 3.5 O or N around Cu at 1.92 Å. Neither EXAFS exhibit second shell coordination in the 2.5−3.0 Å range. RDFs from AIMD performed at 473 K on $Z[Cu^{II}(OH)(NH_3)_3]$ and $Z_2[Cu^{II}(NH_3)_4]$, corresponding to the oxidized 1Al and 2Al species at SCR conditions, are also shown in Figure 10. As with Cu^I, both are free from framework oxygen and remain fully coordinated to NH_3 through the course of the dynamics. RDFs integrate to ~3.9CN; weighting the AIMD RDFs by the XANES-observed fractions of Cu^I and Cu^{II} recovers average coordination numbers of 3.2 and 3.6, close to the EXAFS-fitted values. These species were roughly 50% less mobile than their $Cu^I(NH_3)_2$ counterparts (Table 2), and 30% more mobile than their hydrated forms (Table 2).

Finally, to confirm the transferability of EXAFS spectra collected under the noncatalytic NO + NH_3 and O_2 + NH_3 conditions to catalytic ones, we obtained 473 K SCR operando EXAFS on the recently enhanced APS Sector 10-ID beamline on a Si:Al = 25, Cu:Al = 0.42 sample similar to the 1Al catalyst (Figure 4); kinetic details and spectra are provided in Supporting Information 2.3.5-2. This catalyst has a 60/40 Cu^I/Cu^{II} ratio, a fit CN of 3.1, and no second shell structure. The CN is consistent with a 60/40 weighted average of 2CN Cu^I and 4CN Cu^{II}. The lack of second shell character demonstrates all Cu are NH_3 solvated under operando conditions.

2.4. SCR Mechanism. *2.4.1. $Cu^{II} \rightarrow Cu^I$ Half-Cycle.* We previously proposed an NO-assisted NH_3 dissociation to be responsible for the Cu^{II} to Cu^I reduction during SCR.[83] We report in Figure 14 and Supporting Information 2.4.1-1 the computed CI-NEB pathways for such a step starting from NH_3-saturated Cu^{II} identified in the XAS and DFT here. Both reactions proceed by attack of NO on a Cu-bound NH_3 to form an N−N bond. In the process, a proton is transferred to an acceptor and an electron to Cu, leaving an H_2NNO intermediate that can decompose via proton transfers to N_2 and H_2O.[83,117] In the 1Al case, the Cu−OH ligand acts as the proton acceptor, to form water:

$$Z[Cu^{II}(OH)(NH_3)_3] + NO$$
$$\rightarrow Z[Cu^I(NH_3)_2(H_2NNO)] + H_2O \qquad (14)$$
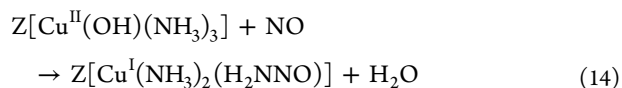
In the 2Al case, an O_f plays the role of the acceptor, to form a new, proximal Brønsted site:

Figure 13. Cu positions (gray balls) sampled inside the zeolite cage during 90 ps of equilibrated NVT AIMD at 473 K for the most stable NH_3 solvated Cu^I and Cu^{II} species.

The four panels are labeled: $Z_2[Cu^{II}(NH_3)_4]$, $Z[Cu^{II}(OH)(NH_3)_3]$, $Z[Cu^I(NH_3)_2]/[ZNH_4]$, $Z[Cu^I(NH_3)_2]$.
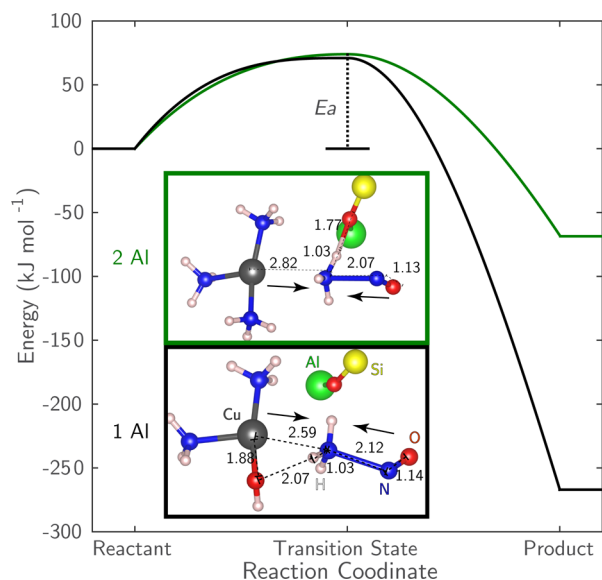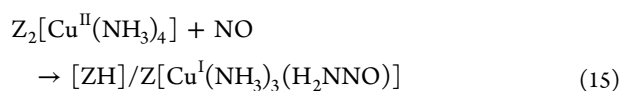
Figure 14. HSE06 CI-NEB calculated activation (E_a) and reaction energies for NO-assisted reduction of NH_3 solvated Cu^{II} 1Al (black) and 2Al (green) sites. Transition state structures are shown boxed. For ease of visualization, most of the zeolite framework is hidden.

$$Z_2[Cu^{II}(NH_3)_4] + NO$$
$$\rightarrow [ZH]/Z[Cu^I(NH_3)_3(H_2NNO)] \quad (15)$$

The first path is much more exothermic than the second (-267 vs -68 kJ mol^{-1}), reflecting the strong driving force for creating H_2O. Nonetheless, the computed barriers for these two paths are a similar 71 and 74 kJ mol^{-1}, respectively, within the HSE06 model. These similarities reflect an early transition state dominated primarily by the partial desorption of NH_3 from Cu to accommodate the attacking NO. The N−N separations at the transition states are over 2 Å, and the N−H bonds are only slightly elongated.

The key difference between the 1Al and 2Al paths is that NH_3/NO reduction of 2Al Cu^{II} should produce new Brønsted sites while 1Al Cu^{II} should not. The number of NH_4^+ species on samples treated in flowing NO and NH_3 (473 K) were counted by TPD performed after purging physisorbed and Cu^I-bound NH_3 species in flowing wet helium (3% H_2O, 433 K).[101] On all Cu-SSZ-13 samples, a larger number of NH_4^+ species were present after reduction treatments than after oxidation treatments (Supporting Information 2.4.1-2). Figure 15 shows the number of additional H^+ sites present after reduction of Cu sites to Cu^I as a function of the Cu:Al ratio on the Si:Al = 5 (blue ◇), 15 (green ○), and 25 (orange □) samples. The dashed lines indicate the excess H^+ expected from the theoretical enumeration of 1Al and 2Al sites (Figure 4). In line with predictions, one additional H^+ site is formed per Cu formed until all of the 2Al sites are filled, beyond which point no additional H^+ sites were formed. Reoxidation in NO and O_2 (Supporting Information 2.4.1-2) returns the samples to the state shown in Figure 5. The catalytic cycle can thus be closed on both 2Al and 1Al sites.

2.4.2. SCR Cycle Energies. The results above highlight the importance of NH_3 coordination during 473 K SCR. We previously proposed an SCR cycle on [Z_2Cu^{II}] sites that accounts for the observed Cu redox.[83] Figure 16 shows an elaboration of that cycle that incorporates NH_3-solvation inferred from the thermodynamic analysis and EXAFS on 1Al
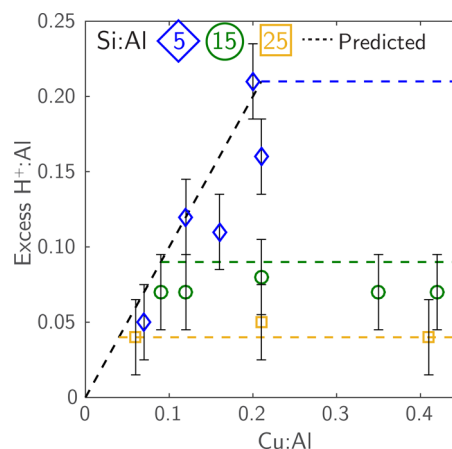

Figure 15. Number of extra H^+ sites (per Al) formed after reduction of Cu^{II} to Cu^I in flowing NO and NH_3 (473 K) as measured by NH_3 titration and TPD. Dashed lines represent the predicted number of H^+ formed on the basis of the assumption that reduction of only Cu^{II} at 2Al sites forms a Cu^I/H^+ site pair.

and 2Al sites. The mechanism includes five primary steps, starting from the 12 o'clock position: (1) NH_3 adsorption on Cu^{II}; (2) NO-assisted NH_3 dissociation concurrent with Cu^{II} reduction to Cu^I; (3) N_2 and H_2O desorption from Cu^I; (4) Cu^I reoxidation to Cu^{II} by NO and O_2 (a nonelementary step); and (5) reaction of adsorbed NO_2 with NH_3 or NH_4^+ to desorb N_2 and H_2O. Figure 16 (right) compares the computed reaction energies for each step (details in Supporting Information 2.4.2-1). The similar energetics are consistent with the similar standard SCR turnover rates (473 K) measured on the two site types (Table 3).

2.5. SCR Rates on Other Cu-Zeolites. All of the cationic Cu species in these cycles are NH_3-solvated and thus not sensitive to the location of charge-compensating framework Al. To test the generality of this observation, standard SCR rates were measured on synthesized and commercial Cu-ZSM-5 and Cu-BEA samples of compositions similar to the Si:Al = 15 SSZ-13 samples. Standard SCR rates (per g, 473 K) on Cu-exchanged MFI (Si:Al = 13), BEA (Si:Al = 13) (sample preparation and characterization described in Supporting Information 5.3-1, 5.3-2, and 2.1.3-1), and Cu-CHA (Si:Al = 5, 15) are shown in Figure 17 as a function of the Cu density (per g). The error was calculated by replicate experiments under the same conditions. These SCR rates were measured in a regime uncorrupted by mass or heat transfer artifacts (Koros-Nowak test[96]) and in a kinetic regime characterized by similar apparent reaction orders and apparent activation energies (Supporting Information 2.5-1). Standard SCR rates (per g, 473 K) increased linearly with Cu density (per g) on the Cu-CHA samples of different Si:Al ratio (5, 15), as expected from the similar turnover rate measured for Cu at 1Al and at 2Al sites (section 2.3.1). Turnover rates for Cu-ZSM-5 and Cu-BEA samples are of the same magnitude and exhibit a similar dependence on Cu density. A linear fit to the entire data set has a correlation coefficient R^2 = 0.86. The Cu speciation was not determined on the Cu-ZSM-5 and Cu-BEA samples, and thus the observed scatter may have contributions from discrepancies between Cu weight % and isolated Cu ion density on these samples. These data suggest that both turnover rates and SCR mechanisms are independent of zeolite support at these conditions and in this kinetic regime. We surmise that this
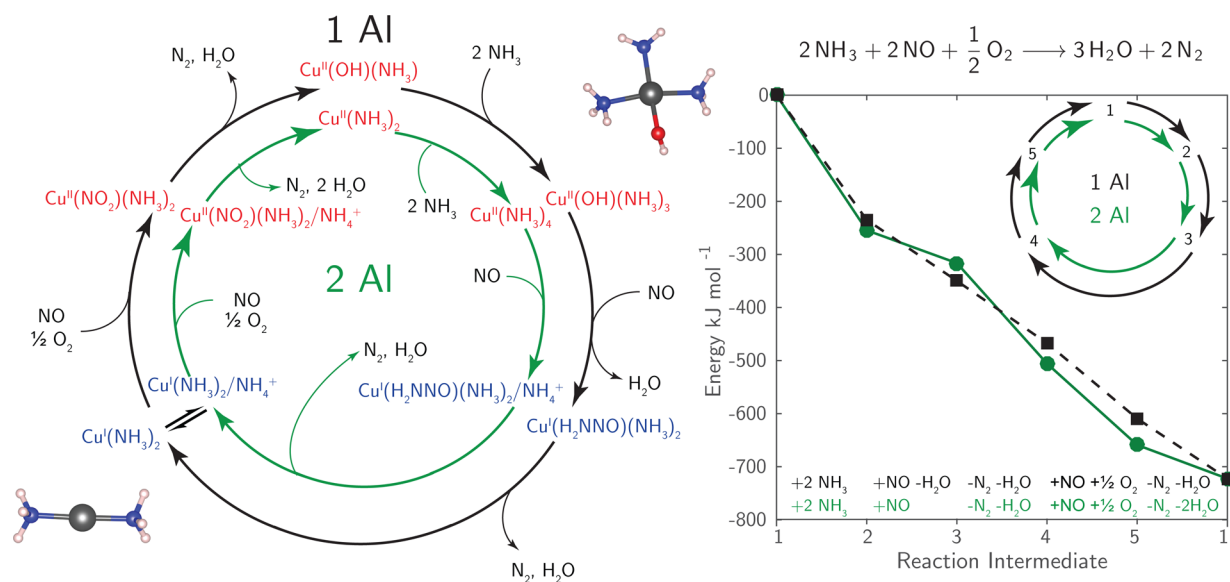
Figure 16. (Left) Proposed parallel standard SCR cycles for NH_3-solvated Cu ions near 1Al (black) or 2Al (green). (Right) HSE06-TSvdw-computed reaction energies along each step of the proposed cycles. 1−5 correspond to the intermediates in the left panel. Listed are the molecules consumed (+) and generated (−) between each intermediate.
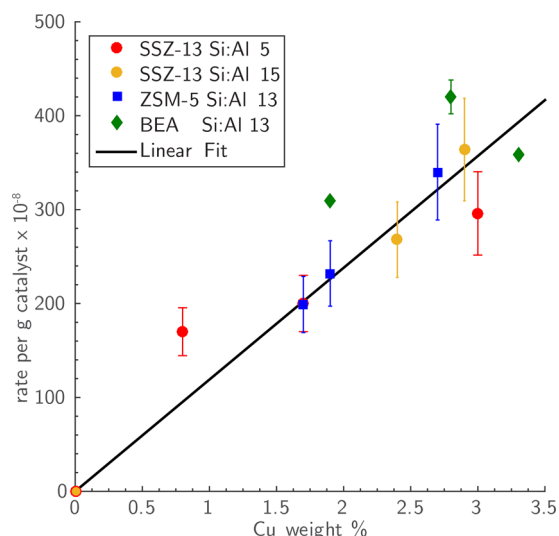

Figure 17. Standard SCR rates per g catalyst at 473 K on Cu-exchanged SSZ-13, ZSM-5, and BEA versus Cu mass density.

insensitivity to zeolite framework arises from NH_3 solvation of both Cu^{II} and Cu^{I} species at 473 K, and that these NH_3-covered ions are responsible for observed SCR turnover.

3. DISCUSSION

3.1. Al Distribution and Cu Speciation Ex Situ. While the apparent macroscopic composition of a heterogeneous catalyst is typically simple to determine, relating that composition to the molecular-scale, functional composition of an active site remains a major challenge. The relevant macroscopic composition variables for the Cu-SSZ-13 materials are the Si:Al and Cu:Al ratios. As reported in Figure 4 and the supporting experimental results, two types of Cu sites are present over the composition ranges studied here, and the relative densities of each type of Cu site are a function of both composition variables. Figure 4 is based on two assumptions: first, that framework Al atoms are randomly sited during zeolite

crystallization modulo Löwenstein's rule, and second, that 6MR 2Al sites are populated by Cu^{II} cations to saturation before 1Al sites are populated with $Cu^{II}OH$. The close correspondence between these predictions and the experimental character-izations supports the model.

Synthesis conditions are well-known to influence Al siting in zeolites,[18,19,45−128] and specifically in SSZ-13,[107] and thus the conclusions drawn from the synthetic conditions here cannot be extended to all Cu-zeolites or even to all Cu-SSZ-13 materials. We can, however, compare our findings to SSZ-13 zeolites prepared via procedures equivalent to those used here.[66,69,100,129−133] Fickel et al.[69] concluded, on the basis of XRD and EXAFS, that an SSZ-13 sample with Si:Al = 9 and Cu:Al = 0.18 contained predominantly Cu in the 6MR, in agreement with the models here that predict 80% of $[Z_2Cu^{II}]$ in such sites. Gao et al. compared the H_2 TPR of SSZ-13 zeolites with Si:Al = 6 and 12 and Cu:Al = 0.10−0.50.[76,77,134] Samples we predict to contain $[Z_2Cu^{II}]$ show only a 653 K TPR feature, while samples in the range expected to contain $[ZCu^{II}OH]$ also exhibit a 503 K TPR feature, consistent with the readier reducibility of $[ZCu^{II}OH]$ sites demonstrated here (Figures 3 and 9). FTIR similarly shows only a 895 cm^{-1} Cu-perturbed T−O−T vibration in the composition range dominated by $[Z_2Cu^{II}]$, supplemented by a 940 cm^{-1} feature in the range containing $[ZCu^{II}OH]$.[134] Davis and co-workers recently showed that these 2Al 6MR sites can be selectively protected against dealumination and deactivated for methanol-to-olefins (MTO) activity by preferential exchange of Cu^{II} ions,[108,135,136] and Gao et al. used an analogous concept to exchange 2Al 6MR sites with alkaline earth cations.[108]

While this partitioning and counting of $[Z_2Cu^{II}]$ and $[ZCu^{II}OH]$ sites is successful, these sites themselves are not monolithic. A 6MR ring can have 2Al in 2NN or 3NN relative positions, and even for given positions, at finite temperature an exchanged ion is quite dynamic within the site, as illustrated by the AIMD simulations. Coordination numbers and bond distances from the HSE06 optimizations are similar to those extracted from the AIMD trajectories, but only the latter captures the contributions of dynamics to the EXAFS. For

example, even for given Al positions within a 6MR, $[Z_2Cu^{II}]$ samples several local minima (Supporting Information 2.2.2-3) during the AIMD, broadening the RDF (Figure 9) and reducing CN < 4. Thus, finite temperatures and Cu dynamics are important considerations in DFT models of these systems.

3.2. Cu Speciation In Situ. Once microscopic sites are identified and enumerated, a second key challenge is to determine how they respond to environmental, in situ conditions. We find from the first-principles thermodynamics and spectroscopies that ambient conditions cause both the $[Z_2Cu^{II}]$ and the $[ZCu^{II}OH]$ species to exist as hydrated ions, liberated from coordination to zeolite framework oxygens, differing in composition by only a single proton, and differing only slightly in mobility (Figure 8). These observations are consistent with a large body of literature on Cu-zeolites. XAS and UV−vis spectroscopies of Cu^{II}-exchanged SSZ-13,[28,71,81,110,137] ZSM-5, and BEA zeolites under ambient conditions are identical to the corresponding spectra of aqueous Cu^{II} complexes, demonstrating the insensitivity of zeolite topology to solvated ions.[71,82] Similarly, the perturbed T−O−T vibrations in IR spectra due to framework-bound Cu^{II} disappear upon hydration of Cu^{II} under ambient conditions.[70] Electron paramagnetic resonance (EPR) spectra at ambient observed for predominantly $[Z_2Cu^{II}]$ samples have been taken as evidence of hydrated and mobile Cu^{II};[77] broadening at 155 K is attributed to loss of that Cu^{II} ion mobility[24,138] and coalescence into a single sharp signal at 523 K to loss of the hydration sphere.[80]

The first-principles thermodynamics and XAS spectroscopies are consistent with the loss of water ligands at high temperature in O_2. Similarly, Borfecchia et al.[64] infer this loss from observed changes in EXAFS to a 3CN Cu species, the same behavior the Si:Al = 15, Cu:Al = 0.44 catalyst exhibits (Figure 9) after dehydration. We and Borfecchia et al. also observe the appearance of Cu^I under more reducing conditions. We assign this reduced fraction to $[ZCu^{II}OH]$ species, based on the comparisons between the 1Al and 2Al samples. The autoreduction is not complete on any sample, suggesting some kinetic in addition to thermodynamic control of the reduction process. The nominal autoreduction stoichiometry:

$$4[ZCu^{II}OH] \rightarrow 4[ZCu^I] + 2H_2O + O_2 \quad (16)$$
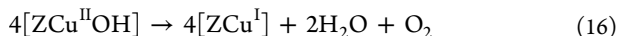
implies a complicated, multistep process likely involving Cu dimer or higher-order intermediates[28,72,77] and thus a sensitivity to spatial Cu−Cu (and hence Al−Al) separations. Consistent with this inference, Gao et al.[76] report that the fraction of reducible $[ZCu^{II}OH]$ at constant Cu:Al ratio decreases with increasing Si:Al ratio, or, equivalently, increasing mean $[ZCu^{II}OH]$ separation.

Under standard SCR conditions at 473 K, Cu^I and Cu^{II} ions near 1Al or 2Al are all predicted and observed to be fully solvated by NH_3, and further all Brønsted sites are present as NH_4^+. Both NH_4^+ and $Cu-NH_3$ are observed in DRIFTS spectra at similar conditions[139−141] on Cu-SSZ-13 samples. In fact, both vibrational and XAS spectra of NH_3 dosed to a number of Cu-exchanged zeolites are similar to those of aqueous $Cu^I(NH_3)_2$ and $Cu^{II}(NH_3)_4$.[66,73,110,140,142−146] The standard SCR active sites at 473 K are NH_3-solvated Cu ions.

NH_3 solvation influences Cu mobility as well as structure, and this effect is insensitive to zeolite topology. NH_3 is observed to promote the exchange of Cu^{II} from $CuO_{(s)}$ into a number of zeolite frameworks, and this process is further promoted by in situ reduction of Cu^{II} to Cu^I by NH_3 and NO mixtures.[116]

3.3. Mechanistic Implications for SCR. The SCR reaction is well established to involve $Cu^I \leftrightarrow Cu^{II}$ redox cycles.[53,73,83,95] There has been some controversy regarding the species responsible for reduction.[56,73,83,90,94] Exposure to NO alone at 473 K does not reduce either the 1Al $[ZCu^{II}OH]$ (Supporting Information 3.4.1-1) or the 2Al $([Z_2Cu^{II}])$[83] samples, and the hybrid-exchange DFT results do not predict NO to strongly bind to or reduce either Cu^{II} site. We thus find no evidence to support the elementary mechanistic steps:

$$[Z_2Cu^{II}] + NO \rightarrow [Z_2Cu^INO^+] \quad (17)$$

or

$$[ZCu^{II}OH] + NO \rightarrow [ZCu^IHONO] \quad (18)$$
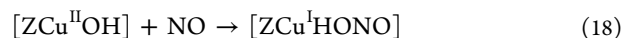
Rather, NO and NH_3 together are necessary to reduce either of these sites. The reaction pathways and activation barriers for these reductions are computed to be similar on the $[ZCu^{II}OH]$ and $[Z_2Cu^{II}]$ sites in the presence of solvating NH_3. These barriers are also similar to the experimental apparent activation energies, although direct comparison of the experiment and computations is only possible through a kinetic model. The presence of both Cu oxidation states during standard SCR likely indicates that neither oxidation nor reduction alone is rate-limiting,[83] and thus a satisfactory kinetic model would require kinetic details on both half-cycles. Reduction rates on the $[ZCu^{II}OH]$ and $[Z_2Cu^{II}]$ may differ at temperatures at which NH_3 ligands are lost.

While NO and NH_3 are most effective at reducing Cu^{II}, we and others[95,147] also observe a partial reduction of $Cu^{II} \rightarrow Cu^I$ in flowing NH_3 and O_2. DFT calculations identified an O_2 assisted NH_3 dissociation pathway that parallels but has a much higher barrier than the NO-assisted NH_3 dissociation reaction.[83] This pathway is unlikely to be catalytically relevant but could be responsible for this reduction.

The results presented here provide indirect mechanistic information about the SCR oxidation half-cycle. We find adsorbed NO_2 to oxidize Cu^I to Cu^{II} as Cu-bound nitrite:

$$Cu^I + NO_2 \rightarrow Cu^{II}O_2N \quad (19)$$
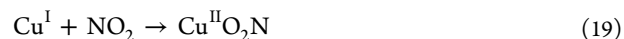
consistent with many proposals.[56,73,91−94] The source of NO_2 and even its presence as a free intermediate during standard SCR is less clear. Janssens et al.[73] proposed NO oxidation to nitrite to occur on a single, reduced Cu site through the intermediacy of a nitrate with the initial step as rate-determining (RDS):

$$[ZCu(O_2)(NO)] \rightarrow [ZCuNO_3] \xrightarrow{+NO} [ZCuNO_2] + NO_2$$
$$\xrightarrow{+NH_3} [ZCuOH] + H_2O + N_2 \quad (20)$$
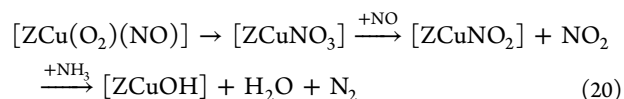
However, computed activation energies and the RDS assumption are inconsistent with experimental activation energies and the observed 50/50 mixture of Cu^I/Cu^{II} for SCR.[66,76,77,83] Rather, as with autoreduction, NO oxidation may involve participation of more than one Cu species, facilitated by the solvation and high mobility of $Cu^I(NH_3)_2$ and its low diffusion barrier between CHA cages. Solvated Cu^I ions are well-known to participate in dimeric Cu oxidation chemistries,[20,148−150] and a second-order dependence of SCR rate on Cu concentration has been observed on an Si:Al = 6 Cu-SSZ-13 catalyst at Cu:Al ratios ≤0.03.[80] At higher temperatures, Cu

is expected to desolvate (Figure 12), consistent with the FTIR findings of Giordanino et al.[139] In sharp contrast to the 473 K spectra (Figure 10), EXAFS collected at 673 K in NH_3 and O_2 demonstrate similar second-shell character (Supporting Information 3.3.3-1) to the dry-oxidized framework bound Cu (Figure 9). Concurrent with this desolvation, apparent activation energies increase from 70 kJ mol^{-1} at 473 K to 140 kJ mol^{-1}[76] at 623 K, consistent with the dip in NO conversion observed[89] in nondifferential measurements. Thus, NH_3 (de)solvation likely has a large impact on SCR oxidation half-cycle rates.

3.4. Implications for Partial Methane Oxidation. The results and approach described here are useful for the interpretation of the recently observed[43] noncatalytic, stoichiometric partial oxidation of methane (PMO) on Cu-SSZ-13:

$$2CH_4 + O_2 \rightarrow 2CH_3OH \qquad (21)$$

PMO is carried out in a three-step sequence[38–41,43] that can be understood in part through reference to Figure 3. In a first step, the Cu-SSZ-13 material is brought to ~673 K in O_2 (~20%) and balance inert, corresponding to condition 2 in the figure. O_2 is then purged by inert, bringing the material to condition 3. We observe a subset of sites to reduce under these conditions, consistent with the participation of only a fraction of exchanged Cu in PMO.[39] Subsequent introduction of CH_4 at 473 K results in the production of methanol, which is liberated by returning to percent level H_2O pressures, between conditions 1 and 2 of Figure 3.

Wulfers et al. demonstrated[43] PMO on Si:Al = 6 and 12, Cu:Al = 0.35 SSZ-13 materials. The Si:Al = 12 sample has roughly double (mol methanol per mol Cu) the performance of the Si:Al = 6 sample, in precise correlation with the predicted increase in $[ZCu^{II}OH]$ sites (Figure 4). We conclude $[ZCu^{II}OH]$ sites are likely precursors to ZCuOCuZ sites proposed to be responsible for PMO activity:[32,35,36,40,42]

$$2ZCuOH \rightarrow ZCuOCuZ + H_2O \qquad (22)$$
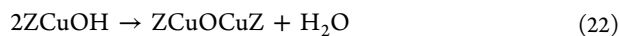
and $[Z_2Cu^{II}]$ sites are inactive.

4. CONCLUSIONS

While the macroscopic composition of a solid catalyst is generally straightforward to measure and control, the relationship between this apparent composition and the number and type of catalytically relevant active sites is generally difficult to infer. We illustrate here an example of a nontrivial catalytic system in which it is possible to determine through theory and experiment both the speciation and the number density of active sites as a function of the relevant synthetic compositional variables. Further, we show that these distinct active sites can be tracked as they evolve under different exposure conditions, from ambient characterization, to dry and inert high temperature, to operando reaction conditions. This enumeration and tracking is enabled by site-sensitive spectroscopies that are able to interrogate the catalyst under working conditions and computational approaches that treat the catalyst in an "operando" fashion, incorporating reaction conditions and effective estimates of free energies avoiding the standard harmonic approximations into the predictions of site structure and composition.

We show that exchanged, atomically dispersed, and isolated Cu ions within the SSZ-13 cages populate two distinct types of sites, distinguished by the number of charge-compensating Al T-sites, and that the structure and dynamics of these two Cu

types are strongly influenced by the environment they experience. H_2O solvates both Cu types at ambient conditions, is lost at higher temperatures, and is replaced by NH_3 reactant at the 473 K SCR conditions. This NH_3 liberates Cu from the framework, greatly enhances Cu mobility, and masks some of the differences between the two site types. The sites remain distinct, however; while both Cu sites undergo similar redox cycles at similar rates under the conditions studied here, the mechanisms differ in detail, as illustrated by the intermediacy of transient Brønsted sites on one but not the other Cu site type (Figure 15).

These findings underscore the need for caution in extrapolating from ex situ characterizations to catalytic conditions. Reaction conditions can and in this example do have a substantial influence on active site structure and properties. These environment-induced modifications need not be limited to reactants. Surrogate "promoters" that modify active sites (e.g., by mobilizing at different conditions, or that modify redox properties) could provide an alternative to traditional catalytic material modifications for tuning catalytic activity.

5. METHODS

5.1. DFT and AIMD Details. Plane-wave, supercell DFT supercell calculations employed a triclinic SSZ-13 supercell containing 12 T-sites[84] and Si:Al ratios of either 11:1 or 10:2. The first Brillouin zone was sampled at the Γ point only, as appropriate for this insulator. Many of the adsorbate structures considered here have multiple local minima. To identify representative structures for subsequent optimizations, initial structures were first annealed nonspin-polarized at 473 K in five independent simulations of 30 ps, each starting from different initial guess structures, for 150 ps total using the Car−Parrinello molecular dynamics software[151](CPMD), version 3.17.1, the Perdew−Becke−Erzenhof[152] generalized gradient approximation (GGA) exchange-correlation functional, and ultrasoft pseudopotentials.[153−155] These Born−Oppenheimer molecular dynamics simulations were run in the NVT ensemble using a Nosé−Hoover thermostat with a time step of 0.6 fs. RDFs from the final 90 of 150 ps simulations were constructed from the trajectories of a subset of these species for comparison to EXAFS results.

Low energy structures visited during the AIMD simulations were subsequently optimized using the Vienna Ab initio Simulation Package (VASP),[156] version 5.3.5. Calculations were performed spin-polarized using the projector augmented wave (PAW) treatment of core−valence interactions[157,158] and a plane wave cutoff of 400 eV. For computational efficiency, structures were first relaxed within the GGA of Perdew et al.[152] and subsequently relaxed using the hybrid screened-exchange method of Heyd−Scuseria−Ernzerhof (HSE06)[159−162] and the Tkatchenko Scheffier method for van der Waals interactions (TS-vdW).[163] We converged self-consistent-field (SCF) electronic energies to 10^{-6} eV and atomic forces to less than 0.03 eV/Å. Charge analysis was performed through the method of Bader.[164−168] Cu charges are reported normalized to Cu^{II} and Cu^I references ($[Z_2Cu^{II}]$ and $[ZCu^I]$, respectively), then rounded to I or II reported as a superscript on Cu. Harmonic vibrational frequencies of adsorbed species were calculated at the HSE06-TSvdW level by numerical differentiation of atomic forces with 0.01 Å displacements on the adsorbate atoms and used to compute zero-point vibrational energies (ZPE). All structures can be found in the Supporting Information sitesCONTCARS attachment.

5.2. Ab Initio Free Energies. To relate DFT-computed energies to reaction conditions, we write the formation energies of adsorbed intermediates[169,170] containing O and H relative to O_2 and H_2O references:

$$\Delta G_{x,y}^{\text{form}}(T, \Delta\mu_{\text{O}_2}, \Delta\mu_{\text{H}_2\text{O}}) = \Delta E_{x,y}^{\text{form}} - T\Delta S_{x,y}^{\text{ST}}(T)$$
$$- \frac{x}{2}\left(\Delta\mu_{\text{H}_2\text{O}} - \frac{1}{2}\Delta\mu_{\text{O}_2}\right) - \frac{y}{2}\Delta\mu_{\text{O}_2} \quad (23)$$

$$\Delta E_{x,y}^{\text{form}} = E_{Z_*\text{CuH}_x\text{O}_y} - E_{Z_*\text{Cu}} - \frac{x}{2}\left(E_{\text{H}_2\text{O}} - \frac{1}{2}E_{\text{O}_2}\right) - \frac{y}{2}E_{\text{O}_2} \quad (24)$$

The $\Delta\mu$ are free parameters corresponding to the difference in chemical potential between 0 K and the conditions of interest. They can be related to corresponding temperatures and pressures through the ideal gas chemical potential relation. ΔS^{ST} is the difference in entropy between a free and adsorbate-covered site. We have previously found that the harmonic oscillator approximation significantly underestimates actual entropies,[83] consistent with observations made by others.[65,68,171] Comparisons with dynamics simulations suggest a simple heuristic in which the difference is approximated from the Sackur–Tetrode expression:

$$\Delta S_{x,y}^{\text{ST}} = (S_{Z_*\text{CuH}_x\text{O}_y} - S_{Z_*\text{Cu}}) \approx \frac{2}{3}k_B \ln\left[\left(\frac{2\pi M_{x,y}k_B T}{h^2}\right)^{3/2}\frac{Ve^{5/2}}{N_A}\right] \quad (25)$$

where $M_{x,y}$ is the total mass of the adsorbed species and V is the supercell volume. This model roughly treats adsorbed species as retaining 2/3 of their gas-phase translational entropy, similar to that discovered for adsorbates at surfaces.[172]

It is straightforward to extend these expressions to ones appropriate in the presence of NH_3, conditions that present nitrogen as well as hydrogen and oxygen to the sites:

$$\Delta G_{x,y,z}^{\text{form}}(T, \Delta\mu_{\text{O}_2}, \Delta\mu_{\text{H}_2\text{O}}, \Delta\mu_{\text{NH}_3}) = \Delta E_{x,y,z}^{\text{form}} - T\Delta S_{x,y,z}^{\text{ST}}(T)$$
$$- \frac{x}{2}\left(\Delta\mu_{\text{H}_2\text{O}} - \frac{1}{2}\Delta\mu_{\text{O}_2}\right) - \frac{y}{2}\Delta\mu_{\text{O}_2}$$
$$- z\left(\Delta\mu_{\text{NH}_3} - \frac{3}{2}\Delta\mu_{\text{H}_2\text{O}} + \frac{3}{4}\Delta\mu_{\text{O}_2}\right) \quad (26)$$

We retain O_2 and H_2O as oxygen and hydrogen references and adopt NH_3 as nitrogen references.

5.3. Zeolite Synthesis and Characterization. Synthesis methods for all zeolites (SSZ-13, BEA, ZSM-5) can be found in Supporting Information 5.3-1. The crystal topologies of H-zeolites were confirmed from powder X-ray diffraction (XRD) patterns collected on a Rigaku SmartLab X-ray diffractometer equipped with a Cu K X-ray source (1.76 kW), and measured from 4° to 40° at a scan rate of 0.00833° s^{-1} with a step size of 0.01° (Supporting Information 2.1.3-1). Micropore volumes of H-SSZ-13 zeolites were determined from Ar adsorption isotherms (87 K), and for H-BEA and H-ZSM-5 zeolites were determined from N_2 adsorption isotherms (77 K), using a Micromeritics ASAP 2020 Surface Area and Porosity Analyzer, and were in reasonable agreement with the values expected for the CHA, BEA, and MFI frameworks and can be found in Supporting Information 5.3-2. Solid-state ^{27}Al magic angle spinning nuclear magnetic resonance (^{27}Al MAS NMR) spectroscopy was used to estimate the fraction of framework and extraframework Al on H-form zeolites. SS NMR spectra were collected using a Chemagnetics CMX400 400 MHz spectrometer in a wide-bore 9.4 T magnet at ambient conditions from 456 scans with 12.5 μs pulses and a 2 s delay and were measured at 104.24 MHz and MAS rate of 5 kHz. Prior to packing in a 4 mm ZrO_2 rotor, zeolite samples were hydrated by holding for >48 h in a desiccator containing a saturated potassium chloride (KCl) solution. All ^{27}Al MAS NMR spectra are referenced to an aqueous 1.0 M $Al(NO_3)_3$ solution. NMR spectra and quantification of extraframework Al for all H-zeolite samples can be found in Supporting Information 5.3-3.

Cu-zeolites were prepared by aqueous-phase Cu ion exchange of H-form zeolites with a $Cu^{II}(NO_3)_2$ solution (0.001–0.1 M, 100 cm^3 g catalyst^{-1}; 99.999 wt %, Sigma-Aldrich) for 4 h and 300 rpm at

ambient conditions, during which the pH was controlled to 4.9 ± 0.1 through dropwise addition of a 1.0 M NH_4OH solution (Sigma-Aldrich). Co-SSZ-13 zeolites were prepared by ion exchange of H-SSZ-13 with an aqueous 0.25 M $Co^{II}(NO_3)_2$ solution (150 mL g catalyst^{-1}) for 4 h at ambient conditions, during which the pH was not controlled (pH stabilized between 3.2 and 3.6 after 4 h). Metal-exchanged zeolites were recovered by centrifugation and washed with deionized water six times (70 mL g catalyst^{-1} per wash), dried at ambient temperature under flowing air, and then treated in flowing dry air (100 mL g catalyst^{-1}) to 773 K (0.0167 K s^{-1}) for 4 h. Elemental composition (Si, Al, Cu, Co) was determined using atomic absorption spectroscopy (AAS) on a PerkinElmer Analyst 300.

5.4. NH₃ Temperature-Programmed Desorption. Residual H$^+$ sites on H-zeolites, on Cu- and Co-exchanged zeolites after oxidation treatments in air (20% O_2, balance N_2, 773 K, 4 h), and on Cu-zeolites after reduction treatments (500 ppm of NO + 500 ppm of NH_3, balance He, 473 K, 2 h) were titrated using the procedure described by Di Iorio et al.[101] This titration method involves saturation of zeolites (~0.03–0.05 g) with NH_3 at 433 K (500 ppm, balance He, 2 h, 350 mL min^{-1}), followed by removal of physisorbed and Cu-bound NH_3 by treatment in wet helium (2.5–3.0% H_2O/He, 8 h, 350 mL min^{-1}), to selectively retain surface NH_4^+ species.[101,102] NH_3 was then evolved in a subsequent TPD in flowing He (350 mL min^{-1}) to 823 K (0.083 K s^{-1}), and quantified using on-board calibrations in a MKS MultiGas 2030 gas-phase FT-IR spectrometer. Further details can be found in Supporting Information 5.4-1.

5.5. Kinetics. Standard selective catalytic reduction (SCR) kinetics were measured on a benchtop tubular glass reactor described elsewhere.[66] All samples were sieved to a nominal size of 125–250 μm and diluted with silica gel to obtain a bed height of ~2.5 cm. Steady-state kinetic data were collected at NO conversions below 20%, so that the entire bed was exposed to approximately the same gas concentrations, using a reactant gas mixture of 300 ppm of NO (3.6% NO/Ar, Praxair), 300 ppm of NH_3 (3.0% NH_3/Ar, Praxair), 5% CO_2 (liquid, Indiana Oxygen), 10% O_2 (99.5%, Indiana Oxygen), 2.5% H_2O (deionized, 18.2 MΩ, introduced through saturator), and balance N_2 (99.999% UHP, Indiana Oxygen) at 473 K and 1 atm. The total gas flow rate was maintained at 1.5 L min^{-1}. Outlet gas concentrations were analyzed using on-board gas calibrations on an MKS MultiGas 2030 gas-phase Fourier transform infrared (FTIR) spectrometer, and NO, NO_2, NH_3, CO_2, and H_2O concentration data were recorded every 0.95 s.

5.6. Spectroscopic Methods (XAS, FTIR). XAS experiments were carried out on the insertion device (ID) and bending magnet (BM) beamlines of the Materials Research Collaborative Access Team (MRCAT, Sector 10) at the Advanced Photon Source (APS) at Argonne National Laboratory. A cryogenically cooled double-crystal Si(111) monochromator was used with an uncoated glass mirror to minimize the presence of harmonics. Spectra were recorded in transmission mode with the ionization chambers optimized for the maximum current with linear response (~1010 photons s^{-1}) using gas mixtures to give 10% absorption in the incident X-ray detector and 70% absorption in the transmission X-ray detector. A Cu metal foil spectrum was simultaneously collected while measuring sample spectra to calibrate the Cu K-edge to 8979 eV. Operando experiments were performed at the 10-ID line in a special glassy carbon tube reactor described by Kispersky et al.,[110] in which XAS spectra were collected simultaneously with steady-state standard SCR rate measurements to verify that rates were identical to those measured in separate differential plug-flow reactor experiments. XAS spectra were collected in an energy range between 8700 and 9890 eV for samples held under different gas conditions, and between 8700 and 9780 eV for operando experiments (additional details in Supporting Information 2.2.1-1). Multiple energy scans were taken to ensure the absence of time-dependent change or beam damage to the sample. Spectra were collected under isothermal conditions and normalized using a first-order polynomial in the pre-edge region and a third-order polynomial in the post-edge region. XANES spectra were fitted using a linear combination of Cu^I and Cu^{II} references[66,83,84] to determine the fractions of Cu^I and Cu^{II} in certain gas environments and under

operando conditions. EXAFS data were fit from $k = 2.7$ to ∼11 Å^{-1} (details of the fitting procedure in Supporting Information 2.2.1-1).

FTIR data were collected on zeolite samples using a Nicolet 6700 FTIR spectrometer equipped with a liquid nitrogen-cooled mercury cadmium telluride (MCT) detector. Catalyst samples (∼35−40 mg) were pressed into a self-supporting wafer (∼2 cm in diameter) and placed in a custom-built FTIR cell that has been described elsewhere.[173] Wafers were treated in flowing oxygen (10% O_2, balance He) to 673 K for 30 min and then cooled to 473 K, prior to collecting spectra. Spectra were collected with a resolution of 4 cm^{-1} and averaged over 1000 scans, baseline corrected, and normalized to the framework Si−O−Si combination/overtone band between 2100 and 1750 cm^{-1}. Additional details can be found in Supporting Information 2.1.3-3.

ASSOCIATED CONTENT

ⓈSupporting Information

The Supporting Information is available free of charge on the ACS Publications website at DOI: 10.1021/jacs.6b02651.

> Additional supplementary details referred to in the main text (PDF)
> Attachment containing geometries of all computed species (ZIP)

AUTHOR INFORMATION

Corresponding Author
*wschneider@nd.edu

Notes
The authors declare no competing financial interest.

ACKNOWLEDGMENTS

REFERENCES

(1) Taylor, H. S. *Proc. R. Soc. London, Ser. A* **1925**, *108*, 105−111.
(2) Behrens, M.; Studt, F.; Kasatkin, I.; Kühl, S.; Hävecker, M.; Abild-Pedersen, F.; Zander, S.; Girgsdies, F.; Kurr, P.; Kniep, B.-L.; Tovar, M.; Fischer, R. W.; Nørskov, J. K.; Schlögl, R. *Science* **2012**, *336*, 893−897.
(3) Zambelli, T.; Wintterlin, J.; Trost, J.; Ertl, G. *Science* **1996**, *273*, 1688−1690.
(4) Jaramillo, T. F.; Jørgensen, K. P.; Bonde, J.; Nielsen, J. H.; Horch, S.; Chorkendorff, I. *Science* **2007**, *317*, 100−102.
(5) Thomas, J. M. *Angew. Chem., Int. Ed.* **1999**, *38*, 3588−3628.
(6) Kim, Y. D.; Seitsonen, A. P.; Wendt, S.; Wang, J.; Fan, C.; Jacobi, K.; Over, H.; Ertl, G. *J. Phys. Chem. B* **2001**, *105*, 3752−3758.
(7) Tyo, E. C.; et al. *ACS Catal.* **2012**, *2*, 2409−2423.
(8) Hwang, T.; Goldsmith, B. R.; Peters, B.; Scott, S. L. *Inorg. Chem.* **2013**, *52*, 13904−13917.
(9) Beale, A. M.; van der Eerden, A. M. J.; Kervinen, K.; Newton, M. A.; Weckhuysen, B. M. *Chem. Commun.* **2005**, 3015−3017.
(10) Topsøe, H. *J. Catal.* **2003**, *216*, 155−164.
(11) Weckhuysen, B. M. *Phys. Chem. Chem. Phys.* **2003**, *5*, 4351−4360.
(12) Green, I. X.; Tang, W.; Neurock, M.; Yates, J. T. *Science* **2011**, *333*, 736−739.
(13) Boubnov, A.; Carvalho, H. W. P.; Doronkin, D. E.; Günter, T.; Gallo, E.; Atkins, A. J.; Jacob, C. R.; Grunwaldt, J.-D. *J. Am. Chem. Soc.* **2014**, *136*, 13006−13015.
(14) Peterson, E. J.; DeLaRiva, A. T.; Lin, S.; Johnson, R. S.; Guo, H.; Miller, J. T.; Kwak, J. H.; Peden, C. H. F.; Kiefer, B.; Allard, L. F.; Ribeiro, F. H.; Datye, A. K. *Nat. Commun.* **2014**, *5*, 4885.
(15) Rice, M. J.; Chakraborty, A. K.; Bell, A. T. *J. Catal.* **2000**, *194*, 278−285.
(16) Rice, M. J.; Chakraborty, A. K.; Bell, A. T. *J. Catal.* **1999**, *186*, 222−227.
(17) Goodman, B. R.; Hass, K. C.; Schneider, W. F.; Adams, J. B. *Catal. Lett.* **2000**, *68*, 85−93.
(18) Sarv, P.; Fernandez, C.; Amoureux, J.-P.; Keskinen, K. *J. Phys. Chem.* **1996**, *100*, 19223−19226.
(19) Perea, D. E.; Arslan, I.; Liu, J.; Ristanović, Z.; Kovarik, L.; Arey, B. W.; Lercher, J. A.; Bare, S. R.; Weckhuysen, B. M. *Nat. Commun.* **2015**, *6*, 7589.
(20) Vanelderen, P.; Vancauwenbergh, J.; Sels, B. F.; Schoonheydt, R. A. *Coord. Chem. Rev.* **2013**, *257*, 483−494.
(21) Rice, M. J.; Chakraborty, A. K.; Bell, A. T. *J. Phys. Chem. B* **2000**, *104*, 9987−9992.
(22) Hass, K. C.; Schneider, W. F. *J. Phys. Chem.* **1996**, *100*, 9292−9301.
(23) Trout, B. L.; Chakraborty, A. K.; Bell, A. T. *J. Phys. Chem.* **1996**, *100*, 4173−4179.
(24) Kucherov, A. V.; Slinkin, A. A.; Kondrat'ev, D. A.; Bondarenko, T. N.; Rubinstein, A. M.; Minachev, K. *Zeolites* **1985**, *5*, 320−324.
(25) Spoto, G.; Zecchina, A.; Bordiga, S.; Ricchiardi, G.; Martra, G.; Leofanti, G.; Petrini, G. *Appl. Catal., B* **1994**, *3*, 151−172.
(26) Palomino, G. T.; Fisicaro, P.; Bordiga, S.; Zecchina, A.; Giamello, E.; Lamberti, C. *J. Phys. Chem. B* **2000**, *104*, 4064−4073.
(27) Nachtigallová, D.; Nachtigall, P.; Sierka, M.; Sauer, J. *Phys. Chem. Chem. Phys.* **1999**, *1*, 2019−2026.
(28) Verma, A. A.; Bates, S. A.; Anggara, T.; Paolucci, C.; Parekh, A. A.; Kamasamudram, K.; Yezerets, A.; Miller, J. T.; Delgass, W. N.; Schneider, W. F.; Ribeiro, F. H. *J. Catal.* **2014**, *312*, 179−190.
(29) Da Costa, P.; Modén, B.; Meitzner, G. D.; Lee, D. K.; Iglesia, E. *Phys. Chem. Chem. Phys.* **2002**, *4*, 4590−4601.
(30) Goodman, B. R.; Hass, K. C.; Schneider, W. F.; Adams, J. B. *J. Phys. Chem. B* **1999**, *103*, 10452−10460.
(31) Smeets, P. J.; Hadt, R. G.; Woertink, J. S.; Vanelderen, P.; Schoonheydt, R. A.; Sels, B. F.; Solomon, E. I. *J. Am. Chem. Soc.* **2010**, *132*, 14736−14738.
(32) Woertink, J. S.; Smeets, P. J.; Groothaert, M. H.; Vance, M. A.; Sels, B. F.; Schoonheydt, R. A.; Solomon, E. I. *Proc. Natl. Acad. Sci. U. S. A.* **2009**, *106*, 18908−18913.
(33) Groothaert, M. H.; van Bokhoven, J. A.; Battiston, A. A.; Weckhuysen, B. M.; Schoonheydt, R. A. *J. Am. Chem. Soc.* **2003**, *125*, 7629−7640.
(34) Balasubramanian, R.; Smith, S. M.; Rawat, S.; Yatsunyk, L. A.; Stemmler, T. L.; Rosenzweig, A. C. *Nature* **2010**, *465*, 115−119.
(35) Groothaert, M. H.; Smeets, P. J.; Sels, B. F.; Jacobs, P. A.; Schoonheydt, R. A. *J. Am. Chem. Soc.* **2005**, *127*, 1394−1395.
(36) Vanelderen, P.; Hadt, R. G.; Smeets, P. J.; Solomon, E. I.; Schoonheydt, R. A.; Sels, B. F. *J. Catal.* **2011**, *284*, 157−164.
(37) Beznis, N. V.; Weckhuysen, B. M.; Bitter, J. H. *Catal. Lett.* **2010**, *138*, 14−22.
(38) Alayon, E. M. C.; Nachtegaal, M.; Bodi, A.; van Bokhoven, J. A. *ACS Catal.* **2014**, *4*, 16−22.
(39) Alayon, E. M. C.; Nachtegaal, M.; Kleymenov, E.; van Bokhoven, J. A. *Microporous Mesoporous Mater.* **2013**, *166*, 131−136.

(40) Alayon, E. M. C.; Nachtegaal, M.; Bodi, A.; Ranocchiari, M.; van Bokhoven, J. A. *Phys. Chem. Chem. Phys.* **2015**, *17*, 7681−7693.

(41) Grundner, S.; Markovits, M. A.; Li, G.; Tromp, M.; Pidko, E. A.; Hensen, E. J.; Jentys, A.; Sanchez-Sanchez, M.; Lercher, J. A. *Nat. Commun.* **2015**, *6*, 7546.

(42) Smeets, P. J.; Groothaert, M. H.; Schoonheydt, R. A. *Catal. Today* **2005**, *110*, 303−309.

(43) Wulfers, M. J.; Lobo, R. F.; Ipek, B.; Teketel, S. *Chem. Commun.* **2015**, *51*, 4447−4450.

(44) King, S. *J. Catal.* **1996**, *161*, 530−538.

(45) Dědeček, J.; Čapek, L.; Sazama, P.; Sobalík, Z.; Wichterlová, B. *Appl. Catal., A* **2011**, *391*, 244−253.

(46) Smeets, P. J.; Sels, B. F.; van Teeffelen, R.; Leeman, H.; Hensen, E. J.; Schoonheydt, R. A. *J. Catal.* **2008**, *256*, 183−191.

(47) Modén, B.; Da Costa, P.; Fonfé, B.; Lee, D. K.; Iglesia, E. *J. Catal.* **2002**, *209*, 75−86.

(48) Iwamoto, M.; Furukawa, H.; Mine, Y.; Uemura, F.; Mikuriya, S.-i.; Kagawa, S. *J. Chem. Soc., Chem. Commun.* **1986**, 1272−1273.

(49) Kamasamudram, K.; Currier, N. W.; Chen, X.; Yezerets, A. *Catal. Today* **2010**, *151*, 212−222.

(50) Grossale, A.; Nova, I.; Tronconi, E.; Chatterjee, D.; Weibel, M. *J. Catal.* **2008**, *256*, 312−322.

(51) Colombo, M.; Nova, I.; Tronconi, E. *Catal. Today* **2010**, *151*, 223−230.

(52) Shishkin, A.; Kannisto, H.; Carlsson, P.-A.; Härelind, H.; Skoglundh, M. *Catal. Sci. Technol.* **2014**, *4*, 3917−3926.

(53) Doronkin, D. E.; Casapu, M.; Günter, T.; Müller, O.; Frahm, R.; Grunwaldt, J.-D. *J. Phys. Chem. C* **2014**, *118*, 10204−10212.

(54) Cavataio, G.; Girard, J.; Patterson, J. E.; Montreuil, C.; Cheng, Y.; Lambert, C. K. *SAE Tech. Pap. Ser.* **2007**, *2007*, 776−790.

(55) Koebel, M.; Elsener, M.; Kleemann, M. *Catal. Today* **2000**, *59*, 335−345.

(56) Brandenberger, S.; Kröcher, O.; Tissler, A.; Althoff, R. *Catal. Rev.: Sci. Eng.* **2008**, *50*, 492−531.

(57) Kwak, J. H.; Tonkyn, R. G.; Kim, D. H.; Szanyi, J.; Peden, C. H. F. *J. Catal.* **2010**, *275*, 187−190.

(58) Ye, Q.; Wang, L.; Yang, R. T. *Appl. Catal., A* **2012**, *427−428*, 24−34.

(59) Luo, J.; Wang, D.; Kumar, A.; Li, J.; Kamasamudram, K.; Currier, N.; Yezerets, A. *Catal. Today* **2015**, *267*, 3−9.

(60) Chen, H.-Y. In *Urea-SCR Technology for deNOx After Treatment of Diesel Exhausts*; Nova, I., Tronconi, E., Eds.; Fundamental and Applied Catalysis; Springer: New York, 2014; pp 123−147.

(61) Baerlocher, C.; McCusker, L. B. Database of Zeolite Structures, 2016; http://www.iza-structure.org/databases/.

(62) Deka, U.; Lezcano-Gonzalez, I.; Warrender, S. J.; Lorena Picone, A.; Wright, P. A.; Weckhuysen, B. M.; Beale, A. M. *Microporous Mesoporous Mater.* **2013**, *166*, 144−152.

(63) Deka, U.; Juhin, A.; Eilertsen, E. A.; Emerich, H.; Green, M. A.; Korhonen, S. T.; Weckhuysen, B. M.; Beale, A. M. *J. Phys. Chem. C* **2012**, *116*, 4809−4818.

(64) Borfecchia, E.; Lomachenko, K. A.; Giordanino, F.; Falsig, H.; Beato, P.; Soldatov, A. V.; Bordiga, S.; Lamberti, C. *Chemical Science* **2015**, *6*, 548−563.

(65) Göltl, F.; Sautet, P.; Hermans, I. *Angew. Chem., Int. Ed.* **2015**, *54*, 7799−7804.

(66) Bates, S. A.; Verma, A. A.; Paolucci, C.; Parekh, A. A.; Anggara, T.; Yezerets, A.; Schneider, W. F.; Miller, J. T.; Delgass, W. N.; Ribeiro, F. H. *J. Catal.* **2014**, *312*, 87−97.

(67) Zhang, R.; McEwen, J.-S.; Kollár, M.; Gao, F.; Wang, Y.; Szanyi, J.; Peden, C. H. *ACS Catal.* **2014**, *4*, 4093−4105.

(68) Göltl, F.; Sautet, P.; Hermans, I. *Catal. Today* **2015**, *267*, 41−46.

(69) Fickel, D. W.; Lobo, R. F. *J. Phys. Chem. C* **2010**, *114*, 1633−1640.

(70) Kwak, J. H.; Varga, T.; Peden, C. H. F.; Gao, F.; Hanson, J. C.; Szanyi, J. *J. Catal.* **2014**, *314*, 83−93.

(71) Giordanino, F.; Vennestrøm, P. N. R.; Lundegaard, L. F.; Stappen, F. N.; Mossin, S.; Beato, P.; Bordiga, S.; Lamberti, C. *Dalton Transactions* **2013**, *42*, 12741−61.

(72) Godiksen, A.; Stappen, F. N.; Vennestrøm, P. N. R.; Giordanino, F.; Rasmussen, S. B.; Lundegaard, L. F.; Mossin, S. *J. Phys. Chem. C* **2014**, *118*, 23126−23138.

(73) Janssens, T. V. W.; Falsig, H.; Lundegaard, L. F.; Vennestrøm, P. N. R.; Rasmussen, S. B.; Moses, P. G.; Giordanino, F.; Borfecchia, E.; Lomachenko, K. A.; Lamberti, C.; Bordiga, S.; Godiksen, A.; Mossin, S.; Beato, P. *ACS Catal.* **2015**, *5*, 2832−2845.

(74) Vennestrøm, P. N. R.; Katerinopoulou, A.; Tiruvalam, R. R.; Kustov, A.; Moses, P. G.; Concepcion, P.; Corma, A. *ACS Catal.* **2013**, *3*, 2158−2161.

(75) Andersen, C. W.; Bremholm, M.; Vennestrøm, P. N. R.; Blichfeld, A. B.; Lundegaard, L. F.; Iversen, B. B. *IUCrJ* **2014**, *1*, 382−386.

(76) Gao, F.; Washton, N. M.; Wang, Y.; Kollár, M.; Szanyi, J.; Peden, C. H. *J. Catal.* **2015**, *331*, 25−38.

(77) Gao, F.; Walter, E. D.; Karp, E. M.; Luo, J.; Tonkyn, R. G.; Kwak, J. H.; Szanyi, J.; Peden, C. H. F. *J. Catal.* **2013**, *300*, 20−29.

(78) Kwak, J. H.; Tran, D.; Szanyi, J.; Peden, C. H. F.; Lee, J. H. *Catal. Lett.* **2012**, *142*, 295−301.

(79) Kwak, J. H.; Tran, D.; Burton, S. D.; Szanyi, J.; Lee, J. H.; Peden, C. H. *J. Catal.* **2012**, *287*, 203−209.

(80) Gao, F.; Walter, E. D.; Kollar, M.; Wang, Y.; Szanyi, J.; Peden, C. H. *J. Catal.* **2014**, *319*, 1−14.

(81) Dědeček, J.; Wichterlová, B. *J. Phys. Chem. B* **1997**, *101*, 10233−10240.

(82) Fulton, J. L.; Hoffmann, M. M.; Darab, J. G.; Palmer, B. J.; Stern, E. A. *J. Phys. Chem. A* **2000**, *104*, 11651−11663.

(83) Paolucci, C.; Verma, A. A.; Bates, S. A.; Kispersky, V. F.; Miller, J. T.; Gounder, R.; Delgass, W. N.; Ribeiro, F. H.; Schneider, W. F. *Angew. Chem., Int. Ed.* **2014**, *53*, 11828−11833.

(84) McEwen, J.-S.; Anggara, T.; Schneider, W.; Kispersky, V.; Miller, J.; Delgass, W.; Ribeiro, F. *Catal. Today* **2012**, *184*, 129−144.

(85) Göltl, F.; Bulo, R. E.; Hafner, J.; Sautet, P. *J. Phys. Chem. Lett.* **2013**, *4*, 2244−2249.

(86) Göltl, F.; Hafner, J. *J. Chem. Phys.* **2012**, *136*, 064501.

(87) Göltl, F.; Hafner, J. *J. Chem. Phys.* **2012**, *136*, 064502.

(88) Göltl, F.; Hafner, J. *J. Chem. Phys.* **2012**, *136*, 064503.

(89) Beale, A. M.; Gao, F.; Lezcano-Gonzalez, I.; Peden, C. H. F.; Szanyi, J. *Chem. Soc. Rev.* **2015**, *44*, 7371−7405.

(90) Kwak, J. H.; Lee, J. H.; Burton, S. D.; Lipton, A. S.; Peden, C. H. F.; Szanyi, J. *Angew. Chem., Int. Ed.* **2013**, *52*, 9985−9989.

(91) Forzatti, P.; Lietti, L.; Nova, I.; Tronconi, E. *Catal. Today* **2010**, *151*, 202−211.

(92) Colombo, M.; Nova, I.; Tronconi, E. *Catal. Today* **2012**, *197*, 243−255.

(93) Ruggeri, M. P.; Selleri, T.; Colombo, M.; Nova, I.; Tronconi, E. *J. Catal.* **2014**, *311*, 266−270.

(94) Ruggeri, M. P.; Nova, I.; Tronconi, E.; Pihl, J. A.; Toops, T. J.; Partridge, W. P. *Appl. Catal., B* **2015**, *166*, 181−192.

(95) Günter, T.; Carvalho, H. W. P.; Doronkin, D. E.; Sheppard, T.; Glatzel, P.; Atkins, A. J.; Rudolph, J.; Jacob, C. R.; Casapu, M.; Grunwaldt, J.-D. *Chem. Commun.* **2015**, *51*, 9227−9230.

(96) Koros, R. M.; Nowak, E. J. *Chem. Eng. Sci.* **1967**, *22*, 470.

(97) Psofogiannakis, G. M.; McCleerey, J. F.; Jaramillo, E.; van Duin, A. C. T. *J. Phys. Chem. C* **2015**, *119*, 6678−6686.

(98) Clemens, A. K. S.; Shishkin, A.; Carlsson, P.-A.; Skoglundh, M.; Martínez-Casado, F. J.; Matĕtj, Z.; Balmes, O.; Härelind, H. *ACS Catal.* **2015**, *5*, 6209−6218.

(99) Löwenstein, W. *Am. Mineral.* **1954**, *39*, 92−96.

(100) Zones, S. I. Zeolite SSZ-13 and its method of preparation. U.S. Patent 4544538A, 1985.

(101) Di Iorio, J. R.; Bates, S. A.; Verma, A. A.; Delgass, W. N.; Ribeiro, F. H.; Miller, J. T.; Gounder, R. *Top. Catal.* **2015**, *58*, 424−434.

(102) Bates, S. A.; Delgass, W. N.; Ribeiro, F. H.; Miller, J. T.; Gounder, R. *J. Catal.* **2014**, *312*, 26−36.

(103) Sierka, M.; Sauer, J. *J. Phys. Chem. B* **2001**, *105*, 1603−1613.

(104) Smith, L.; Davidson, A.; Cheetham, A. *Catal. Lett.* **1997**, *49*, 143−146.

(105) Bordiga, S.; Vitillo, J. G.; Ricchiardi, G.; Regli, L.; Cocina, D.; Zecchina, A.; Arstad, B.; Bjørgen, M.; Hafizovic, J.; Lillerud, K. F. *J. Phys. Chem. B* **2005**, *109*, 18237−18242.

(106) Baes, C. F.; Mesmer, R. E. *Hydrolysis of Cations*; Wiley: New York, 1976.

(107) Di Iorio, J. R.; Gounder, R. *Chem. Mater.* **2016**, *28*, 2236−2247.

(108) Gao, F.; Wang, Y.; Washton, N. M.; Kollár, M.; Szanyi, J.; Peden, C. H. F. *ACS Catal.* **2015**, *5*, 6780−6791.

(109) Wang, D.; Jangjou, Y.; Liu, Y.; Sharma, M. K.; Luo, J.; Li, J.; Kamasamudram, K.; Epling, W. S. *Appl. Catal., B* **2015**, *165*, 438−445.

(110) Kispersky, V. F.; Kropf, A. J.; Ribeiro, F. H.; Miller, J. T. *Phys. Chem. Chem. Phys.* **2012**, *14*, 2229−2238.

(111) Auroux, A.; Bolis, V.; Wierzchowski, P.; Gravelle, P. C.; Vedrine, J. C. *J. Chem. Soc., Faraday Trans. 1* **1979**, *75*, 2544.

(112) Auroux, A. *Calorimetry and Thermal Methods in Catalysis*; Springer: New York, 2013; Vol. *154*, pp 1−561.

(113) Sharma, S.; Meyers, B.; Chen, D.; Miller, J.; Dumesic, J. *Appl. Catal., A* **1993**, *102*, 253−265.

(114) Lee, C.; Parrillo, D. J.; Gorte, R. J.; Farneth, W. E. *J. Am. Chem. Soc.* **1996**, *118*, 3262−3268.

(115) Brändle, M.; Sauer, J.; Dovesi, R.; Harrison, N. *J. Chem. Phys.* **1998**, *109*, 10379.

(116) Shwan, S.; Skoglundh, M.; Lundegaard, L. F.; Tiruvalam, R. R.; Janssens, T. V.; Carlsson, A.; Vennestrøm, P. N. *ACS Catal.* **2015**, *5*, 16−19.

(117) Sun, D.; Schneider, W. F.; Adams, J. B.; Sengupta, D. *J. Phys. Chem. A* **2004**, *108*, 9365−9374.

(118) Dědeček, J.; Sobalík, Z.; Wichterlová, B. *Catal. Rev.: Sci. Eng.* **2012**, *54*, 135−223.

(119) Pashkova, V.; Klein, P.; Dedecek, J.; Tokarová, V.; Wichterlová, B. *Microporous Mesoporous Mater.* **2015**, *202*, 138−146.

(120) Sklenak, S.; Dědeček, J.; Li, C.; Wichterlová, B.; Gábová, V.; Sierka, M.; Sauer, J. *Phys. Chem. Chem. Phys.* **2009**, *11*, 1237−1247.

(121) Sklenak, S.; Dědeček, J.; Li, C.; Wichterlová, B.; Gábová, V.; Sierka, M.; Sauer, J. *Angew. Chem., Int. Ed.* **2007**, *46*, 7286−7289.

(122) Dědeček, J.; Kaucký, D.; Wichterlová, B.; Gonsiorová, O. *Phys. Chem. Chem. Phys.* **2002**, *4*, 5406−5413.

(123) Gábová, V.; Dědeček, J.; Čejka, J. *Chem. Commun.* **2003**, 1196−1197.

(124) Vjunov, A.; Fulton, J. L.; Huthwelker, T.; Pin, S.; Mei, D.; Schenter, G. K.; Govind, N.; Camaioni, D. M.; Hu, J. Z.; Lercher, J. A. *J. Am. Chem. Soc.* **2014**, *136*, 8296−306.

(125) Akporiaye, D. E.; Dahl, I. M.; Mostad, H. B.; Wendelbo, R. *J. Phys. Chem.* **1996**, *100*, 4148−4153.

(126) Prasad, S.; Petrov, M. *Solid State Nucl. Magn. Reson.* **2013**, *54*, 26−31.

(127) Han, O. H.; Kim, C. S.; Hong, S. B. *Angew. Chem., Int. Ed.* **2002**, *41*, 469−472.

(128) Yokoi, T.; Mochizuki, H.; Namba, S.; Kondo, J. N.; Tatsumi, T. *J. Phys. Chem. C* **2015**, *119*, 15303−15315.

(129) Eilertsen, E. A.; Arstad, B.; Svelle, S.; Lillerud, K. P. *Microporous Mesoporous Mater.* **2012**, *153*, 94−99.

(130) Fickel, D. W.; D'addio, E.; Lauterbach, J. A.; Lobo, R. F. *Appl. Catal., B* **2011**, *102*, 441−448.

(131) Zones, S. I. *J. Chem. Soc., Faraday Trans.* **1991**, *87*, 3709−3716.

(132) Zones, S.; Van Nordstrand, R. *Zeolites* **1988**, *8*, 166−174.

(133) Chang, C.-C.; Wang, Z.; Dornath, P.; Cho, J. H.; Fan, W. *RSC Adv.* **2012**, *2*, 10475−10477.

(134) Kwak, J. H.; Zhu, H.; Lee, J. H.; Peden, C. H. F.; Szanyi, J. *Chem. Commun.* **2012**, *48*, 4758−4760.

(135) Dusselier, M.; Deimund, M. A.; Schmidt, J. E.; Davis, M. E. *ACS Catal.* **2015**, *5*, 6078−6085.

(136) Deimund, M. A.; Harrison, L.; Lunn, J. D.; Liu, Y.; Malek, A.; Shayib, R.; Davis, M. E. *ACS Catal.* **2016**, *6*, 542−550.

(137) Groothaert, M.; Lievens, K.; Van Bokhoven, J.; Battiston, A.; Weckhuysen, B.; Pierloot, K.; Schoonheydt, R. *Stud. Surf. Sci. Catal.* **2004**, *154 C*, 2449−2457.

(138) Kucherov, A. V.; Slinkin, A. A. *Zeolites* **1986**, *6*, 175−180.

(139) Giordanino, F.; Borfecchia, E.; Lomachenko, K. A.; Lazzarini, A.; Agostini, G.; Gallo, E.; Soldatov, A. V.; Beato, P.; Bordiga, S.; Lamberti, C. *J. Phys. Chem. Lett.* **2014**, *5*, 1552−1559.

(140) Zhu, H.; Kwak, J. H.; Peden, C. H. F.; Szanyi, J. *Catal. Today* **2013**, *205*, 16−23.

(141) Szanyi, J.; Kwak, J. H.; Zhu, H.; Peden, C. H. F. *Phys. Chem. Chem. Phys.* **2013**, *15*, 2368−2380.

(142) Lamble, G.; Moen, A.; Nicholson, D. G. *J. Chem. Soc., Faraday Trans.* **1994**, *90*, 2211−2213.

(143) Wang, D.; Zhang, L.; Kamasamudram, K.; Epling, W. S. *ACS Catal.* **2013**, *3*, 871−881.

(144) Sjövall, H.; Fridell, E.; Blint, R. J.; Olsson, L. *Top. Catal.* **2007**, *42*, 113−117.

(145) Lezcano-Gonzalez, I.; Deka, U.; Arstad, B.; Van Yperen-De Deyne, A.; Hemelsoet, K.; Waroquier, M.; Van Speybroeck, V.; Weckhuysen, B. M.; Beale, A. M. *Phys. Chem. Chem. Phys.* **2014**, *16*, 1639−1650.

(146) Gomez-Lor, B.; Iglesias, M.; Cascales, C.; Gutierrez-Puebla, E.; Monge, M. A. *Chem. Mater.* **2001**, *13*, 1364−1368.

(147) Moreno-González, M.; Hueso, B.; Boronat, M.; Blasco, T.; Corma, A. *J. Phys. Chem. Lett.* **2015**, *6*, 1011−1017.

(148) Hoover, J. M.; Ryland, B. L.; Stahl, S. S. *J. Am. Chem. Soc.* **2013**, *135*, 2357−67.

(149) Chen, P.; Solomon, E. I. *Proc. Natl. Acad. Sci. U. S. A.* **2004**, *101*, 13105−13110.

(150) Solomon, E. I.; Heppner, D. E.; Johnston, E. M.; Ginsbach, J. W.; Cirera, J.; Qayyum, M. F.; Kieber-Emmons, M. T.; Kjaergaard, C. H.; Hadt, R. G.; Tian, L. *Chem. Rev.* **2014**, *114*, 3659−3853.

(151) CPMD, http://www.cpmd.org/, Copyright IBM Corp 1990−2016, Copyright MPI für Festkörperforschung Stuttgart 1997−2001.

(152) Perdew, J. P.; Wang, Y. *Phys. Rev. B: Condens. Matter Mater. Phys.* **1992**, *45*, 13244−13249.

(153) Vanderbilt, D. *Phys. Rev. B: Condens. Matter Mater. Phys.* **1990**, *41*, 7892−7895.

(154) Laasonen, K.; Car, R.; Lee, C.; Vanderbilt, D. *Phys. Rev. B: Condens. Matter Mater. Phys.* **1991**, *43*, 6796−6799.

(155) Laasonen, K.; Pasquarello, A.; Car, R.; Lee, C.; Vanderbilt, D. *Phys. Rev. B: Condens. Matter Mater. Phys.* **1993**, *47*, 10142−10153.

(156) Kresse, G.; Furthmüller, J. *Phys. Rev. B: Condens. Matter Mater. Phys.* **1996**, *54*, 11169−11186.

(157) Blöchl, P. E. *Phys. Rev. B: Condens. Matter Mater. Phys.* **1994**, *50*, 17953−17979.

(158) Kresse, G.; Joubert, D. *Phys. Rev. B: Condens. Matter Mater. Phys.* **1999**, *59*, 1758−1775.

(159) Heyd, J.; Scuseria, G. E.; Ernzerhof, M. *J. Chem. Phys.* **2003**, *118*, 8207−8215.

(160) Heyd, J.; Scuseria, G. E. *J. Chem. Phys.* **2004**, *121*, 1187−1192.

(161) Heyd, J.; Scuseria, G. E.; Ernzerhof, M. *J. Chem. Phys.* **2006**, *124*, 219906.

(162) Krukau, A. V.; Vydrov, O. A.; Izmaylov, A. F.; Scuseria, G. E. *J. Chem. Phys.* **2006**, *125*, 224106.

(163) Tkatchenko, A.; Scheffler, M. *Phys. Rev. Lett.* **2009**, *102*, 73005.

(164) Bader, R. F. W. *Atoms in Molecules a Quantum Theory*, Oxford University Press, 1990.

(165) Tang, W.; Sanville, E.; Henkelman, G. *J. Phys.: Condens. Matter* **2009**, *21*, 084204.

(166) Sanville, E.; Kenny, S. D.; Smith, R.; Henkelman, G. *J. Comput. Chem.* **2007**, *28*, 899−908.

(167) Henkelman, G.; Arnaldsson, A.; Jónsson, H. *Comput. Mater. Sci.* **2006**, *36*, 354−360.

(168) Yu, M.; Trinkle, D. R. *J. Chem. Phys.* **2011**, *134*, 064111.

(169) Bray, J. M.; Schneider, W. F. In *Chapter 2. First-principles Thermodynamic Models in Heterogeneous Catalysis*; Asthagiri, A., Janik, M., Eds.; Royal Society of Chemistry: UK, 2013; pp 59−115.

(170) Penninger, M. W.; Kim, C. H.; Thompson, L. T.; Schneider, W. F. *J. Phys. Chem. C* **2015**, *119*, 20488−20494.

(171) Piccini, G.; Sauer, J. *J. Chem. Theory Comput.* **2014**, *10*, 2479−2487.

(172) Campbell, C. T.; Sellers, J. R. V. *J. Am. Chem. Soc.* **2012**, *134*, 18109−18115.

(173) Wang, J.; Kispersky, V. F.; Delgass, W. N.; Ribeiro, F. H. *J. Catal.* **2012**, *289*, 171−178.

■ NOTE ADDED AFTER ASAP PUBLICATION

This manuscript published ASAP on 4/29/2016. The Supporting Information file was replaced and the revised version was reposted on 5/2/16.